12-2023

Model of Surface Waves on a Viscoelastic Material in a Cylindrical Container with Edge Constraints

Phillip Wilson
pcwilso@clemson.edu

Model of surface waves on a viscoelastic material in a cylindrical container with edge constraints

---

A Dissertation
Presented to
the Graduate School of
Clemson University

In Partial Fulfillment
of the Requirements for the Degree
Master of Science
Mechanical Engineering

---

by
Phillip Wilson
December 2023

Accepted by:
Dr. Joshua Bostwick, Committee Chair
Dr. John Saylor
Dr. Xiangchun Xuan

Abstract

A theoretical model is developed for the resonant frequencies and mode shapes of pinned edge surface waves on a viscoelastic fluid contained in a finite depth cylindrical container. A boundary integral approach is used to map the governing equations to the domain boundary. The surface waves obey an eigenvalue operator equation that depends on four dimensionless parameters: the cylinder aspect ratio, the Bond number, the Ohnesorge number, and the elastocapillary number. A solution is constructed using a Rayleigh-Ritz variational procedure over a constrained function space, which is able to effectively incorporate the pinned edge boundary condition. Mode shapes are defined by the mode number pair (n, m), where n is the radial mode number and m is the azimuthal mode number. The focus is on irrotational motions, but we show that rotational effects only affect the dissipation in the system. The theoretical predictions agree well with related experiments over a wide range of material parameters.

Dedication

This work is dedicated to my beautiful wife, Sierra, and to my daughter, Lucy.

Acknowledgments

Many people have been a part of making this research a success. Thank you first and foremost to my advisor, Dr. Bostwick. You have provided invaluable guidance and support and devoted much time to working with me on this research. Countless issues and difficulties have been overcome through your insight. I have been fortunate to have you as an advisor and mentor. Thank you also to my other committee members, Dr. Saylor and Dr. Xuan.

A special thanks is due to my brother Daniel Wilson, who has always provided a listening ear and offered insight into my research. We have spent many an hour discussing what we are learning and bouncing ideas off of each other.

I owe many thanks to my family for their constant and unceasing support. Thank you to my other siblings, Catherine, Joseph, Nathan, Cindy, Isabella, Juliana, Gabriella, Nora Grace, Jonathan, and Stephen Wilson. Most importantly, thank you to my parents, John and Tina Wilson. You have been a constant rock of support, and I owe so much of my success to you. I would not be where I am today were it not for your love and encouragement.

Finally, thank you to my patient and supportive wife, Sierra. She has been my biggest supporter, patiently encouraging and pushing me to excellence. I am blessed to have you by my side.

Table of Contents

Title Page . . . . . **i**

Abstract . . . . . **ii**

Dedication . . . . . **iii**

Acknowledgments . . . . . **iv**

List of Tables . . . . . **vii**

List of Figures . . . . . **viii**

1 Introduction **1**
1.1 Background 2
1.2 Experimental Motivation 4
1.3 Theoretical Approach 5
1.4 Chapter Overview 7

2 Irrotational Theory **8**
2.1 Derivation of governing equations 8
2.2 Free solution 20
2.3 Forced solution 21

3 Results and Experimental Comparison **23**
3.1 Theoretical Results 23
3.2 Experimental Comparison 36
3.3 Viscous Variation Comparison 40
3.4 Elastic Variation Comparison 41
3.5 Height Variation Comparison 41
3.6 Pinned vs. Sliding Comparison 42

4 Rotational Theory **44**
4.1 Derivation of governing equations 44
4.2 Results and comparison 58

5 Conclusion **62**

Appendices **65**
A Derivation of the free surface curvature 66
B MATLAB Code for Rayleigh-Ritz Solution Method 68
C MATLAB Code for Parameter Analysis 81
D MATLAB Code for Mode Visualization 97

Bibliography 111

List of Tables

3.1 Pinned condition dimensionless natural frequencies for various modes. Calculations are for water in an infinite depth cylinder ($h = \infty$, $Bo = 167$, $Oh = 6 \times 10^{-4}$). . . . 25
3.2 Sliding condition dimensionless natural frequencies for various modes. Calculations are for water in an infinite depth cylinder ($h = \infty$, $Bo = 167$, $Oh = 6 \times 10^{-4}$). . . . 25
3.3 Pinned condition dimensionless natural frequencies of various modes for water with $h = 0.629$. 39
3.4 Pinned condition dimensionless natural frequencies of various modes for different glycerol/water ratios with $h = 0.629$. 40
3.5 Pinned condition dimensionless natural frequencies of various modes for different agarose gels with $h = 0.629$. 41
3.6 Pinned condition dimensionless natural frequencies of various modes for different glycerol/water ratios with $h = 0.629$. 42
3.7 Pinned condition dimensionless natural frequencies of various modes for different glycerol/water ratios with $h = 0.2$. 42
3.8 Pinned and sliding dimensionless natural frequencies of various modes for a Triton/water solution with $h = 0.629$. 42

4.1 Real and imaginary frequencies for the first six axisymmetric modes from both irrotational and rotational analysis. Computations are for water at room temperature. . 59

List of Figures

1.1 Example of experimentally observed surface wave patterns defined by an (n, m) mode number. 4

2.1 System definition sketch. 9

3.1 Illustration of various modes. (a)-(c) show the first three axisymmetric modes where $n = 1, 2, 3$, while (d)-(f) show modes with azimuthal waves where $m = 1, 2, 3$. 24
3.2 Illustration of the shape, pressure field, and velocity field of the first three axisymmetric modes (1,0), (2,0), and ((3,0). In (d)-(f), the light yellow indicates high pressure, while the dark blue indicates low pressure. 27
3.3 Semilog plot showing how the dimensionless frequency λ changes as the cylinder aspect ratio h varies ($Oh = 0$, $Ec = 0$, $Bo = 0$). 28
3.4 Semilog plot showing how the dimensionless frequency λ changes as the Bond number Bo varies ($h = \infty$, $Oh = 0$, $Ec = 0$). 29
3.5 Semilog plot showing how the dimensionless frequency λ changes as the elastocapillary number Ec varies ($h = \infty$, $Oh = 0$, $Bo = 0$). 30
3.6 Comparison of real and imaginary frequencies as the Ohnesorge number Oh is varied for the first three modes ($h = \infty$, $Ec = 0$, $Bo = 0$). 31
3.7 Curves representing the transition from underdamped to overdamped in relation to the elastocapillary number Ec and the Ohnesorge number Oh for the first five modes ($h = \infty$, $Bo = 0$). 32
3.8 Forced amplitude response as the nondimensional frequency λ is increased for $m = 0$. 33
3.9 Comparison of the the first peak ($n = 1$) for several azimuthal modes. 34
3.10 Example of how the forced response changes as the Ohnesorge number Oh is varied. 35
3.11 Example of how the forced response changes as the elastocapillary number Ec is varied. 36
3.12 Illustration of the shape and corresponding wave slope contour image for various modes. (a)-(f) show the first three axisymmetric modes where $n = 1, 2, 3$, while (g)-(l) show modes with azimuthal waves where $m = 1, 2, 3$. 38

4.1 System definition sketch. 45
4.2 Comparison of the irrotational and rotational frequency response as the Ohnesorge number is varied for the first axisymmetric mode ($n = 1$). 60
4.3 Comparison of the irrotational and rotational forced amplitude response as the nondimensional frequency λ is increased. 61

Chapter 1

Introduction

There are numerous applications in which pattern formation on the surface of a liquid has been utilized, such as spray cooling [1] and drop atomization for drug delivery [2] [3] [4]. Chen *et al.* [5] has demonstrated that wave patterns can be used to assemble microscale materials into ordered structures. In particular, surface wave patterns have been used to assemble organoid cells in the bioengineering of 3D microtissues [6] with application to bottom-up tissue engineering [7]. Typically a soft gel such as agarose or alginate is used in these bioengineering technologies [8] [9]. It has been shown that surface waves in a brimful cylindrical tank can be used as a DNA biosensor by relating the surface rheology to biomolecules [10] [11]. Particle redistribution using Faraday waves has been explored by Wright and Saylor [12] and Saylor and Kinard [13]. Strickland *et al.* [14] has investigated the dynamics of insoluble surfactant density redistribution driven by gravity-capillary waves in a cylindrical container. Surface waves have been used to reorder layers of granular media [15] and create turbulent mixing of two miscible fluids [16]. Liquid and surfactant properties have also both been measured using edge waves [17] [18].

In these applications, understanding and controlling pattern formation on a liquid/gas interface is necessary. To that end, extensive experimental study of surface waves on viscoelastic fluids in a cylinder with various boundary conditions has been conducted by Dr. Xingchen Shao. Motivated by this experimental work, in this thesis a theoretical model is developed for surface waves on a viscoelastic fluid in a finite depth cylindrical container.

1.1 Background

The study of surface waves on a fluid in a container originated with Faraday and his experiments in 1831 [19]. He observed that vertically oscillated fluids form standing surface waves, and his observation was that these waves appear at half of the driving frequency, which is known as a sub-harmonic response. Study of this phenomena was continued by Mathiessen in 1868 [20] [21], who observed a waves with a harmonic response (equal to the driving frequency), and Rayleigh in 1883 [22] [23], who observed sub-harmonic surface waves like Farady. Theoretical understanding of surface waves was significantly advanced in 1954 through the work of Benjamin and Ursell [24], who applied linear stability analysis to the problem of inviscid fluid in an oscillating cylinder and derived the Mathieu equation. The Mathieu equation defines when surface waves will appear though "tongues" of instability in terms of the driving frequency and amplitude. This analysis showed that Faraday waves can exhibit a subharmonic, harmonic, or superharmonic response. Typically the subharmonic instability tongue requires the lowest onset acceleration, which is why sub-harmonic Faraday waves are most frequently observed experimentally. It should be noted, however, that there are exceptions where another instability tongue has a lower onset acceleration. For example, in thin viscous fluid layers the harmonic instability tongue can have a lower onset acceleration [25] [26]. In addition, oscillating a container of fluid with multiple driving frequencies has been observed to create complex quasi-patterns [27] [28].

In addition to Faraday waves, harmonic edge waves can also appear on a fluid surface, generally at lower driving amplitudes. These capillary-gravity waves are caused by the meniscus at the contact line between the container and the free surface of the fluid, and are defined by a balance between the fluid inertia and the forces of surface tension and gravity (which act as restorative forces in the system). In 1932, Lamb [29] showed that capillary-gravity waves can be characterized by a dispersion relationship with a continuous spectrum. Provided a meniscus and a pinned contact line are present, vertical oscillations of a container create waves that propagate from the walls to the center of the container. If the forcing amplitude is below the Faraday wave threshold, the edge waves will exhibit a harmonic response [19] [24]. In the case of a cylindrical container in particular, at a resonance frequency, radially propagating edge waves will constructively interact to create a standing wave defined by a fixed number of circular nodes. In some cases this can lead to mode mixing, where a combination of Faraday waves and edge waves are observed. If pure Faraday waves are of interest,

edge waves can been suppressed in several ways in experimental investigations. Christiansen *et al.* [30] accomplished this by using a container with a large aspect ratio, while Bechhoefer *et al.* [31] used a highly viscous fluid that caused the edge waves to become over-damped. Soluble surfactants have also been used to creating a sliding (unpinned) meniscus [32] [33], suppressing edge wave formation. However, if high enough driving frequencies are applied, neither container geometry nor the edge conditions affect the surface wave formation [27].

It has been shown that for a finite sized tank, capillary-gravity waves tend to conform to the geometry of the container [34] [35], and it has likewise been shown that for small containers, Faraday waves tend to conform to the container geometry [36] [37]. In the case of a cylindrical container, this means that the surface waves are can be described by an integer-valued mode number pair (n, m), where n is the radial mode number and m is the azimuthal mode number, and each mode has a finite bandwidth over which it can be excited [32]. Henderson and Miles [38] have experimentally measured the resonance frequencies and decay rates for surface waves in a brimful cylindrical container. In finite sized cylindrical containers, it has been demonstrated that there can be interaction between two modes with very similar frequencies, leading to chaotic dynamics [39] [40] [41]. Henderson and Miles [38] have theoretically modeled a first-order approximation of the cylinder assuming a fixed contact line (pinned edge condition) and Stokes boundary layers. Their predictions of natural frequencies and damping rations have been further developed by Martel, Nicolas, and Vega [42] to include higher order viscous effects. The decay rate due to viscous dissipation within the bulk liquid was further considered by Miles and Henderson [43].

For low mode number shapes, dissipation due to contact-line motion can be comparable to bulk viscous dissipation [44] [45] [46], so contact line conditions are an important consideration. Contact-line dissipation can be avoided by enforcing either a pinned contact line or a free sliding contact line, the two limiting cases of contact line motion. Experimentally, a pinned contact line can be created by filling a container brimful, and a free sliding contact line can be achieved by using surfactants [32] or by using two or more immiscilbe liquids [47] [48]. It has been shown by Kidambi [49] that for a viscous liquid, the spectrum is affected by the value of the static contact angle. The large Bond number limit for an inviscid fluid was analyzed by Nicolás [50], in which both the free sliding and pinned edge contact line conditions were compared. It was demonstrated by Kidambi [51] that even in an inviscid fluid there is damping due to dynamic wetting effects (contact line motion). Michel, Pétrélis and Fauve [52] have recently shown that the presence of a meniscus

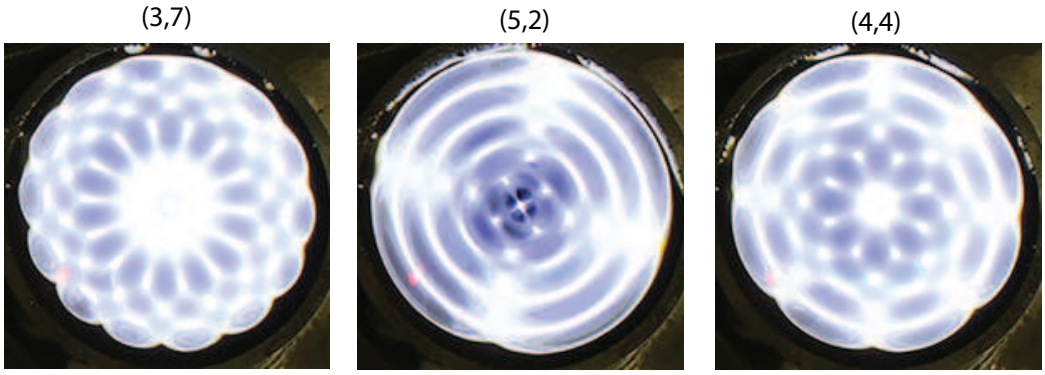

Figure 1.1: Example of experimentally observed surface wave patterns defined by an (n, m) mode number.

can cause surface wave damping. The review articles by Miles and Henderson [53] and Perlin and Schultz [54] can be referenced for an overview of the literature on surface waves.

1.2 Experimental Motivation

In the experimental work of Dr. Xingchen Shao, extensive experimental observations were made of surface waves generated by mechanically vibrating liquid in a cylinder with a flat, brimful pinned edge condition and an angled meniscus edge condition [55] [56] [57] [58] [59]. Several examples of these surface wave patterns are shown in Figure 1.1 [57]. These experiments were used to identify the first 50 resonance modes of pure water (along with more complex mixed mode patterns involving multiple waves with different dynamics). The theoretical model presented in this thesis shows excellent agreement with those experimental works.

Further experiments were performed using viscoelastic materials to explore the effect of material properties on surface waves. While Faraday waves have been widely studied for Newtonian fluids [36] [60] [30] [27] [61] [54] [62], there has been far less investigation of complex viscoelastic fluids. Viscoelastic materials are characterized by displaying both viscous and elastic behavior, which is defined by a complex modulus $G' + iG''$. Rheological tests are used to evaluate this complex modulus [63]. The elastic behavior is defined by the storage modulus G', while the viscous behavior is defined by the loss modulus iG''. While these properties are typically dependent on the frequency of applied shear, materials where used in the experiments that have constant rheological properties over the range of driving frequencies that were applied. Experimentally, the elastic and

viscous material properties were isolated by using two different materials. Glycerol/water mixtures were used to vary the loss modulus iG'' (viscosity) with negligible elasticity, as the elastic behavior is negligible compared to the viscous behavior. Agarose gels were used to vary the shear modulus G with relatively low viscosity, since aragose gels generally fall into the category of 'inviscid elastic fluids,' where G' is orders of magitude greater than G'' [64] [65] [66]. Surface waves on aragose gels fall into the category of elastocapillarity, where the elastic and surface tension forces are comparable [67] [68] [69] [65] [66] [59]. Elastocapillary effects are known to affect the wave response in classical hydrodynamic instabilities including drop oscillations [70] [71], Plateau-Rayleigh instability [72], and Rayleigh-Taylor instability [73]. By varying concentrations in the glycerol/water mixtures and agarose gels used, rheological properties were manipulated to explore viscous and elastic effects over a wide range of values.

1.3 Theoretical Approach

In terms of theoretical modeling, the dynamics of surface waves can be broadly characterized by an operator equation of the following form [46]:

$$\lambda^2 M + \lambda L + R = K \tag{1.1}$$

Here λ is the scaled driving frequency, M is the liquid inertia operator, L is the dissipation operator (viscosity), R is the restorative force operator (including surface tension, gravity, and elasticity), and K is the driving amplitude. In this work, a model of this form is derived which is dependent on four dimensionless parameters: the aspect ratio (h), the Bond number (Bo), the Ohnesorge number (Oh), and the elastocapillary number (Ec).

The contact line is of important consideration in developing a theoretical model. If motion of the contact line is allowed (i.e. the contact line is sliding and the contact angle can vary), dynamic wetting effects can be introduced, causing contact-line dissipation even for inviscid liquids. This was first discovered by Davis [44] and Hocking [45], and Davis showed that this is a purely dissipative feature of the system [44]. Consequently, contact line dissipation can be accounted for in the dissipation operator L, often by introducing a constitutive law relating the contact angle and the contact line speed. Lyubimov *et al.* [74] and Bostwick and Steen [75] have studied the effect of contact line dissipation on frequency response for driven sessile drops.

In most of the experiments that motivate the theoretical study presented here, a pinned contact line is enforced. As such, the theoretical model is developed to include a pinned edge condition. However, the theoretical modeling of surface waves with a pinned contact line presents a difficulty because a pinned edge condition is incompatible with the no-penetration condition at the sidewall of the container. The natural boundary condition for this problem is an orthogonal sliding contact line, where the slope of the free surface is always zero at the contact line, but the contact line can "slide" vertically up and down the container wall. This allows for a much simpler analysis in which a spacial normal mode to be factored through the governing equations, giving a purely time-dependent equation and the dispersion relationship. For the pinned edge case, the incompatible boundary conditions result in an over constrained problem, and there have been several approaches employed to resolve this issue.

A variational approach with a Lagrange multiplier was used by Benjamin and Scott to analyze pinned edge surface waves in narrow open channels with rectangular geometry [76], and this analysis was expanded by Graham-Eagle to model a brimful, pinned edge, infinite depth cylinder [77]. Another approach, proposed by Prosperetti, is to create a pinned contact line by introducing a singular pressure term at the contact line [78], allowing for a similar analysis to the typical methods used for the unconstrained problem (see [29] and [79]). Finally, Bostwick and Steen have used a Rayleigh–Ritz variational procedure over a constrained function space to analyze capillary oscillations of constrained drops [80] [81] [82] and bridges [83] [84], and that is the approach that is used here.

While most of the research to date has focused on inviscid or viscous fluids, the model that is developed here accounts for both viscous and elastic effects, which allows for theoretical modeling of viscous fluids, elastic gels, and fluids that exhibit viscoelastic behavior. The theoretical model predicts the natural frequencies for modes with both radial and azimuthal waves, in addition to including the effect of a finite cylinder depth. The model shows excellent agreement between the predicted resonance frequencies and the experimentally observed mode frequencies. This theoretical work, along with the corresponding experimental study, has been published in three journal papers [57] [56] [55].

1.4 Chapter Overview

Chapter 2 presents the derivation of the theoretical model for surface waves on a cylindrical container assuming irrotational flow. Both the free and forced responses of the system are modeled with a pinned edge contact line, and the dispersion relationship is derived for the sliding contact line condition. In Chapter 3, the theory is extensively compared to experimental results to validate the model. Comparison is made with experiments varying all of the dimensionless parameters (h, Bo, Oh, Ec) for both axisymmetric and nonaxisymmetric modes, as well as both pinned and sliding contact lines. It is demonstrated that the theory shows excellent agreement with experimental observations. The effects of varying the dimensionless parameters are also analyzed. In Chapter 4, a model is derived allowing for rotational flow in the fluid. While the majority of research assumes irrotational flow, this research explores the effects of including fluid rotation through this second model. The model predicts the natural frequencies for axisymmetric modes for an infinite depth cylinder, and the results are compared with the irrotational theory. Finally, concluding remarks are presented in Chapter 5.

Chapter 2

Irrotational Theory

In this chapter, the theoretical model is derived for surface waves on a viscoelastic fluid in a cylinder, assumming irrotational flow and incorporating a pinned edge boundary condition.

2.1 Derivation of governing equations

The problem definition sketch is shown in Figure 2.1. A cylindrical container of fluid is considered, of height L, where the container is filled to the brim, creating a pinned edge boundary condition at $r = a$. The area above the fluid surface is filled with a passive gas that does not affect the dynamics of the system. A small perturbation $\eta(r, \theta, t)$ is applied to the free surface of the fluid, such that the height of the free surface, the fluid pressure, and the fluid velocity can be defined in terms of base quantities of $O(1)$ and perturbed quantities of $O(\varepsilon)$.

$$z = L + \varepsilon\eta \tag{2.1a}$$

$$P = P_0 + \varepsilon P \tag{2.1b}$$

$$\mathbf{u} = \mathbf{u}_0 + \varepsilon\mathbf{u} \tag{2.1c}$$

Here the base height of the interface is simply the height of the cylinder L. Since the fluid is exposed at the free surface, the base pressure P_0 is equal to the pressure of the gas. The unperturbed fluid

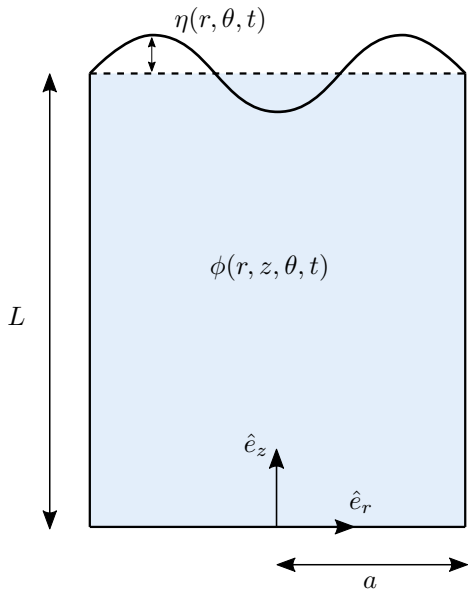

Figure 2.1: System definition sketch.

is static, so the base velocity $\mathbf{u}_0 = 0$. Lengths are nondimensionalized by the radius a:

$$r^* = \frac{r}{a} \rightarrow r = r^* a \tag{2.2a}$$

$$z^* = \frac{z}{a} \rightarrow z = z^* a \tag{2.2b}$$

For the time being η is kept in dimensional form. Here an aspect ratio is naturally introduced, which is defined as

$$h = \frac{L}{a}. \tag{2.3}$$

For simplicity, r, z, and η will refer to the dimensionless radius, height, and disturbance. We thus have that $r \in [0, 1]$ and $z \in (0, h)$.

2.1.1 Conservation of mass

The two field equations governing the system are conservation of mass (continuity) and conservation of momentum (Navier-Stokes). Assuming the fluid is incompressible, continuity dictates

that the divergence of the velocity must equal zero. Hence we have:

$$\nabla \cdot \mathbf{u} = 0 \tag{2.4}$$

Further assuming that the flow is irrotational, the velocity field can be described by a velocity potential, where the velocity is equal to the gradient of the potential.

$$\mathbf{u} = \nabla \Phi \tag{2.5}$$

Substituting (2.5) into (4.3) yields Laplace's equation, which governs the velocity potential.

$$\nabla^2 \Phi = 0 \tag{2.6}$$

2.1.2 Conservation of momentum

Conservation of momentum is governed by the incompressible Navier-Stokes equations:

$$\rho \frac{D\mathbf{u}}{Dt} = -\nabla P + \mu \nabla^2 \mathbf{u} + \nabla U \tag{2.7}$$

Here P is the pressure in the fluid, μ is the viscosity, and U is the gravitational potential. The material derivative (left hand side of the equation), can be expanded to

$$\rho \frac{D\mathbf{u}}{Dt} = \rho \frac{\partial \mathbf{u}}{\partial t} + \rho(\mathbf{u} \cdot \nabla)\mathbf{u} \tag{2.8}$$

However, in the linear approximation the convective term is neglected because it is $O(\varepsilon^2)$, so the material derivative reduces to

$$\rho \frac{D\mathbf{u}}{Dt} = \rho \frac{\partial \mathbf{u}}{\partial t} \tag{2.9}$$

Using a vector identity, the viscous term can be expanded as follows:

$$\mu \nabla^2 \mathbf{u} = \mu \left[\nabla(\nabla \cdot \mathbf{u}) - \nabla \times \nabla \times \mathbf{u} \right] \tag{2.10}$$

Continuity states that the divergence of the velocity is equal to zero, which means that the first term disappears and the viscous term becomes

$$\mu\nabla^2\mathbf{u} = -\mu\nabla\times\nabla\times\mathbf{u}. \tag{2.11}$$

The gravitational potential U can be expressed as

$$U = -\rho g z. \tag{2.12}$$

The height z is expressed in (4.1a). Taking only the $O(\epsilon)$ term gives

$$U = -\rho g \eta. \tag{2.13}$$

Substituting (2.9),(2.11), and (2.13) into (2.7), the momentum balance is expressed as

$$\rho\frac{\partial\mathbf{u}}{\partial t} = -\nabla P - \mu\nabla\times\nabla\times\mathbf{u} - \nabla(\rho g\eta). \tag{2.14}$$

Substituting the velocity potential definition (2.5) into (2.14) the viscous term disappears, and factoring out a gradient, the equation is reduced to

$$\rho\frac{\partial\Phi}{\partial t} = -P - \rho g\eta. \tag{2.15}$$

In the case of forced oscillations, a driving pressure must be included in the governing equations, so the pressure in the momentum balance is expanded to

$$P \to P + P_d, \tag{2.16}$$

where P_d is an oscillating pressure imposed on the system by an external force. The momentum balance can thus be expressed as

$$\rho\frac{\partial\Phi}{\partial t} = -P - P_d - \rho g\eta. \tag{2.17}$$

Equations (2.6) and (2.17) govern the fluid motion within the cylinder.

2.1.3 Volume conservation

As the fluid is assumed to be incompressible, a volume constraint must be enforced over the perturbation on the free surface:

$$\int_0^{2\pi} \int_0^1 r\eta\,(r,\theta,t)\,dr d\theta = 0 \tag{2.18}$$

This condition ensures that the mode solutions conserve volume for the fluid in the cylinder.

2.1.4 Normal modes

The time and azimuthal dependency of the velocity potential, fluid pressure, driving pressure, and surface perturbation are separated using normal modes:

$$\Phi(r,z,\theta,t) = \phi(r,z)e^{im\theta}e^{i\omega t} \tag{2.19a}$$

$$P(r,z,\theta,t) = p(r,z)e^{im\theta}e^{i\omega t} \tag{2.19b}$$

$$P_d(r,\theta,t) = p_d(r)e^{im\theta}e^{i\omega t} \tag{2.19c}$$

$$\eta(r,\theta,t) = y(r)e^{im\theta}e^{i\omega t} \tag{2.19d}$$

Substituting (2.19) into (2.6) and (2.17) results in reduced governing equations:

$$\nabla^2\phi = 0 \tag{2.20a}$$

$$i\omega\rho\phi = -p - p_d - \rho g y \tag{2.20b}$$

The volume conservation constraint (2.18) is naturally satisfied for $m \neq 0$, but it is not for $m = 0$. For $m = 0$, the reduced surface perturbation y must satisfy

$$\int_0^1 r y\,(r)dr. \tag{2.21}$$

2.1.5 Boundary conditions

The following boundary conditions are applied at the boundaries of the cylindrical container. No penetration is required on the bottom surface and on the walls of the cylinder:

$$\frac{\partial \phi}{\partial z} = 0 \Big|_{z=0} \tag{2.22a}$$

$$\frac{\partial \phi}{\partial r} = 0 \Big|_{r=1} \tag{2.22b}$$

In addition, there is a kinematic condition at the surface of the fluid, which requires the fluid velocity be equal to the velocity of the surface disturbance:

$$\frac{\partial \phi}{\partial z} = \frac{\partial \eta}{\partial t} \Big|_{z=h} \tag{2.23}$$

Substituting in the normal modes, the kinematic condition becomes

$$\frac{\partial \phi}{\partial z} = i\omega y \Big|_{z=h}. \tag{2.24}$$

Finally, a kinetic condition must be applied at the fluid surface. The difference in normal stresses across the interface is balanced by the curvature of the surface, as described by the Young-Laplace equation

$$\hat{n} \cdot \underline{\underline{T}}^f \cdot \hat{n} - \hat{n} \cdot \underline{\underline{T}}^g \cdot \hat{n} = -\sigma(\nabla \cdot \hat{n}), \tag{2.25}$$

where $\underline{\underline{T}}^f$ is the stress tensor in the fluid, $\underline{\underline{T}}^g$ is the stress tensor in the gas, σ is the surface tension at the interface, $\hat{n}$ is the unit normal vector of the surface (in the positive z direction). If the fluid is Newtonian, the $O(\varepsilon)$ component of the normal stress in the z direction can be expressed as

$$T_{zz} = -p + 2\mu \frac{\partial u_z}{\partial z}. \tag{2.26}$$

The normal stress for the gas is simply $-P_0$, so the $O(\varepsilon)$ component is zero. Thus, the kinetic boundary condition becomes

$$p - 2\mu \frac{\partial u_z}{\partial z} = \sigma(\nabla \cdot \hat{n}). \tag{2.27}$$

Per the derivation in Appendix A, the divergence of the normal is

$$\nabla \cdot \hat{n} = \frac{1}{a^2}\left[-\frac{d^2}{dr^2} - \frac{1}{r}\frac{d}{dr} + \frac{m^2}{r^2}\right] y \tag{2.28}$$

Substituting the velocity potential (2.5) and the curvature (2.28) into (2.27) gives

$$p - 2\mu\frac{\partial^2\phi}{\partial z^2} = -\frac{\sigma}{a^2}\left[\frac{d^2}{dr^2} + \frac{1}{r}\frac{d}{dr} - \frac{m^2}{r^2}\right] y. \tag{2.29}$$

2.1.6 Elasticity

If the fluid exhibits viscoelastic behavior, this can be accounted for by replacing the viscosity μ with a complex version:

$$\mu \to \mu + \frac{G}{i\omega} \tag{2.30}$$

where G is the shear modulus of the liquid. Substituting this expanded viscosity into (2.29) results in a viscoelastic version of the Young-Laplace equation:

$$p - 2\mu\frac{\partial^2\phi}{\partial z^2} - \frac{2G}{i\omega}\frac{\partial^2\phi}{\partial z^2} = -\frac{\sigma}{a^2}\left[\frac{d^2}{dr^2} + \frac{1}{r}\frac{d}{dr} - \frac{m^2}{r^2}\right] y \tag{2.31}$$

Note that if the shear modulus is equal to zero (i.e. the fluid exhibits no elastic behavior), then (2.31) simply reduces to the viscous equation (2.29).

2.1.7 Solution

A solution can be constructed for the velocity potential using separation of variables, where the velocity potential is defined as

$$\phi(r, z) = R(r)Z(z), \tag{2.32}$$

and the solution for $Z(z)$ must be of the form

$$Z(z) = A_n \cosh(k_{mn} z) + B_n \sinh(k_{mn} z). \tag{2.33}$$

Because of the no penetration condition (2.22a) at $z = 0$, it follows that $B_n = 0$, which gives

$$Z(z) = A_n \cosh(k_{mn} z). \tag{2.34}$$

The solution to $R(r)$ is a Bessel function of the form

$$R(r) = J_m(k_{mn}r). \tag{2.35}$$

We let k_{mn} be the nth zero of J'_m in order to satisfy the no penetration condition (2.22b)at $r = 1$. The reduced velocity potential is then

$$\phi(r, z) = \sum_{n=1}^{\infty} A_n \cosh(k_{mn}z) J_m(k_{mn}r) \tag{2.36}$$

Since the Bessel functions appear in the velocity potential, it is natural to construct a solution to the surface disturbance using a Bessel series (use Bessel functions as a basis for y). Due to the orthogonality of the Bessel functions, we can express y as follows:

$$y(r) = \sum_{n=1}^{\infty} C_n J_m(k_{mn}r) \tag{2.37a}$$

$$C_n = \frac{\langle y, J_m(k_{mn}r)\rangle}{\langle J_m(k_{mn}r), J_m(k_{mn}r)\rangle}, \tag{2.37b}$$

where the inner product is defined as

$$\langle f(r), g(r)\rangle = \int_0^1 r f(r) g(r) dr. \tag{2.38}$$

Substituting the disturbance (2.37) and the velocity potential (2.36) into the kinematic condition (2.24), we have

$$\sum_{n=1}^{\infty} \frac{k_{mn}}{a} A_n \sinh(k_{mn}h) J_m(k_{mn}r) = i\omega \sum_{n=1}^{\infty} C_n J_m(k_{mn}r) \tag{2.39a}$$

$$\Rightarrow \frac{k_{mn}}{a} A_n \sinh(k_{mn}h) = i\omega C_n \tag{2.39b}$$

$$\Rightarrow A_n = \frac{i\omega a C_n}{k_{mn} \sinh(k_{mn}h)} \tag{2.39c}$$

Thus, we can express the velocity potential as

$$\phi(r, z) = i\omega \sum_{n=1}^{\infty} \frac{a}{k_{mn}} \frac{\cosh(k_{mn}z)}{\sinh(k_{mn}h)} \frac{\langle y, J_m(k_{mn}r)\rangle}{\langle J_m(k_{mn}r), J_m(k_{mn}r)\rangle} J_m(k_{mn}r). \tag{2.40}$$

We solve for the pressure from the momentum balance (2.20b):

$$p = -i\omega\rho\phi - p_d - \rho g y \tag{2.41}$$

Substituting the velocity potential and pressure into the kinetic boundary condition (2.29) gives

$$-i\omega\rho\phi - p_d - \rho g y - 2\mu\frac{\partial^2\phi}{\partial z^2} - \frac{2G}{i\omega}\frac{\partial^2\phi}{\partial z^2} = -\frac{\sigma}{a^2}\left[\frac{d^2}{dr^2} + \frac{1}{r}\frac{d}{dr} - \frac{m^2}{r^2}\right] y. \tag{2.42}$$

(2.42) is valid at the free surface ($z = h$); hence, the velocity potential is evaluated at the free surface

$$\phi(r,z) = i\omega\sum_{n=1}^{\infty}\frac{a}{k_{mn}}\coth(k_{mn}h)\{y\}J_m(k_{mn}r) \tag{2.43a}$$

$$\{y\} = \frac{\langle y, J_m(k_{mn}r)\rangle}{\langle J_m(k_{mn}r), J_m(k_{mn}r)\rangle} \tag{2.43b}$$

and substituted into the kinetic condition (2.42) to give an integro-differential equation in terms of the velocity potential and the disturbance:

$$\begin{aligned}\rho\omega^2 a\sum_{n=1}^{\infty}\frac{1}{k_{mn}}\coth(k_{mn}h)\{y\}J_m(k_{mn}r)& \\ - i\frac{2\mu\omega}{a}\sum_{n=1}^{\infty}k_{mn}\coth(k_{mn}h)\{y\}J_m(k_{mn}r)& \\ - \frac{2G}{a}\sum_{n=1}^{\infty}k_{mn}\coth(k_{mn}h)\{y\}J_m(k_{mn}r)& \\ - p_d - \rho g y + \frac{\sigma}{a^2}\left[\frac{d^2}{dr^2} + \frac{1}{r}\frac{d}{dr} - \frac{m^2}{r^2}\right] y = 0.&\end{aligned} \tag{2.44}$$

We now scale y by the radius a such that

$$y^* = \frac{y}{a} \rightarrow y = y^* a. \tag{2.45}$$

For simplicity, y^* is denoted as y from now on. Substituting in the scaled disturbance into (2.44)

and dividing through by $\frac{\sigma}{a}$, we have

$$\lambda^2 \sum_{n=1}^{\infty} \frac{1}{k_{mn}} \coth(k_{mn}h)\{y\}J_m(k_{mn}r) - i\lambda 2(Oh) \sum_{n=1}^{\infty} k_{mn} \coth(k_{mn}h)\{y\}J_m(k_{mn}r) - 2(Ec) \sum_{n=1}^{\infty} k_{mn} \coth(k_{mn}h)\{y\}J_m(k_{mn}r) - \hat{p}_d - (Bo)y + \left[\frac{d^2}{dr^2} + \frac{1}{r}\frac{d}{dr} - \frac{m^2}{r^2}\right] y = 0, \quad (2.46)$$

where λ is the dimensionless frequency, Oh is the Ohnesorge number (dimensionless viscosity parameter), Ec is the elastocapillary number (dimensionless elasticity parameter), Bo is the Bond number (dimensionless gravity parameter), and $\hat{p}_d$ is the dimensionless driving pressure, defined as

$$\lambda \equiv \sqrt{\frac{\rho a^3 \omega^2}{\sigma}} \quad (2.47a)$$

$$Oh \equiv \frac{\mu}{\sqrt{\rho \sigma a}} \quad (2.47b)$$

$$Ec \equiv \frac{Ga}{\sigma} \quad (2.47c)$$

$$Bo \equiv \frac{\rho g a^2}{\sigma} \quad (2.47d)$$

$$\hat{p}_d = \frac{p_d a}{\sigma} \quad (2.47e)$$

The kinetic force balance (2.46) can be written as an operator equation of the following form:

$$\lambda^2 M[y] + \lambda L[y; Oh] + R[y; Ec, Bo] = A, \quad (2.48)$$

The operator $M[y]$ is the inertial term, defined as

$$M[\mathrm{y}] \equiv \sum_{n=1}^{\infty} \frac{1}{k_{mn}} \coth(k_{mn}h)\{y\}J_m(k_{mn}r). \quad (2.49)$$

The operator $L[y; Oh]$ is the viscous term, which is introduced through the boundary conditions and causes dissipation in the system:

$$L[\mathrm{y}; Oh] \equiv -i2(Oh) \sum_{n=1}^{\infty} k_{mn} \coth(k_{mn}h)\{y\}J_m(k_{mn}r) \quad (2.50)$$

The operator $R[y; Ec, Bo]$ is related to the elasticity, the gravitational force, and the curvature (i.e. the surface energy) at the interface:

$$R[\mathrm{y}; Ec, Bo] \equiv -2(Ec)\sum_{n=1}^{\infty} k_{mn}\coth(k_{mn}h)\{y\}J_m(k_{mn}r) - (Bo)y + \left[\frac{d^2}{dr^2} + \frac{1}{r}\frac{d}{dr} - \frac{m^2}{r^2}\right]y \quad (2.51)$$

Finally, the A term on the right hand side of the equation is a forcing function, which in this case is simply the driving pressure:

$$A = \hat{p}_d \quad (2.52)$$

The operator equation (4.72) forms a polynomial eigenvalue problem, which governs the dynamics of the system.

2.1.8 Sliding basis functions

As was noted in Figure 2.1, the problem definition sketch, the primary boundary condition we are interested in studying is the pinned edge condition, where the surface disturbance is always equal to zero at the rim of the cylinder:

$$y = 0|_{r=1} \quad (2.53)$$

However, another possible boundary condition is requiring that the derivative of the surface disturbance is equal to zero at the edge of the cylinder:

$$\frac{\partial y}{\partial r} = 0\Big|_{r=1} \quad (2.54)$$

This is a sliding boundary condition, where the fluid contact line can "slide" up and down in the z direction, but the derivative must remain equal to zero at every point on the contact line. In this case, the Bessel functions naturally fulfill the sliding contact line condition (2.54). If we define the surface disturbance y as a series of Bessel functions, as done previously in (2.37), and plug that into the governing equation (2.48) with the driving pressure equal to zero, the result is a relatively simple

equation:

$$\lambda^2 - i\lambda 2(Oh)k_{mn}^2 - 2(Ec)k_{mn}^2 - \tan(k_{mn}h)(Bo + k_{mn}^2) = 0 \tag{2.55}$$

Equation (2.55) is a second order polynomial equation that can easily be solved for the dimensionless frequency λ given the four dimensionless parameters Oh, Ec, Bo, and h, as well as k_{mn}, which corresponds to a specific (n, m) mode. λ represents the natural frequency of the vibrational mode. Thus, equation (2.55) allows for the straightforward calculation of the natural frequencies of different modes with a sliding contact line condition.

2.1.9 Pinned basis functions

Ordinary Bessel functions cannot be used in solving for the pinned edge condition, as these functions do not inherently satisfy equation (2.53). In order to account for this, modified Bessel functions are computed, which are used as basis functions in the Rayleigh-Ritz method solution. The modified Bessel functions are as follows:

$$S_n^m(r) = J_m(k_{mn}r) - \frac{J_m(k_{mn})}{J_m(k_{m1})}J_m(k_{m1}r) \qquad n = 2, 3, ...N \tag{2.56}$$

It can be easily seen that if $r = 1$, S_n^m must necessarily be zero, which creates the required pinned condition. However, S_1^m is zero everywhere, so the function space is reduced to $N - 1$ and n begins counting from 2. In addition, the functions S_n^m are not orthogonal. The Grahm-Schmidt orthogonolization process is used to remedy this. The resulting orthogonal functions that satisfy the pinned edge condition are denoted $V_n^m(r)$, where $n = 1, 2, 3, ...N$ These functions necessarily satisfy

$$\int_0^1 rV_i^m(r)V_j^m(r)dr = 0 \qquad i \neq j \tag{2.57}$$

Thus, for the pinned contact line condition, the surface disturbance can be expressed as a linear combination of these basis functions:

$$y(r) = \sum_{n=1}^{\infty} c_n V_n^m(r) \tag{2.58}$$

It should be noted that these modified basis functions satisfy the volume constraint (2.21) for $m = 0$. This can be shown from the following Bessel identity:

$$\int_0^1 rJ_0\left(kr\right)dr = \frac{-J_0'\left(k\right)}{k^2} \tag{2.59}$$

The k values were defined such that $J' = 0$, which means that for k_{0n}, $J_0' = 0$. Thus, the integral must be equal to zero for any n:

$$\int_0^1 rJ_0\left(kr\right)dr = 0 \tag{2.60}$$

Since the modified basis functions are just a linear combination of the Bessel functions, we can also conclude that

$$\int_0^1 rV_n^0(r)dr = 0. \tag{2.61}$$

Thus, the volume constraint is satisfied by the pinned edge basis functions.

2.2 Free solution

The free solution is when the forcing term in the operator equation (2.48) is zero (i.e. $\hat{p}_d = 0$):

$$\lambda^2 M[y] + \lambda L[y; Oh] + R[y; Ec, Bo] = 0, \tag{2.62}$$

This means that the frequency is an unknown and must be solved for. Using the pinned basis functions (2.58), the integro-differential operator equation (2.62) is difficult to solve analytically; hence, it is numerically solved using the Rayleigh-Ritz method, which approximates the solution to the eigenvalue problem by expressing it as a matrix equation. Each of the operators in (2.48) are transformed into matrices via inner products with the orthogonal basis functions as follows:

$$\left\langle \lambda^2 M[y_i] + \lambda L[y_i] + R[y_i], V_j \right\rangle = 0 \tag{2.63a}$$

$$\Rightarrow c_i \left\langle \lambda^2 M[V_i^m] + \lambda L[V_i^m] + R[V_i^m], V_j^m \right\rangle = 0 \tag{2.63b}$$

where the inner product is defined as (2.38). Thus, the operator equation can be expressed as

$$(\lambda^2 \mathbf{M} + \lambda \mathbf{L} + \mathbf{R})\mathbf{c} = 0, \tag{2.64}$$

where the matrices **M**, **L**, and **R** are defined as

$$\mathbf{M} = \langle M[V_i], V_j \rangle \tag{2.65a}$$

$$\mathbf{L} = \langle L[V_i], V_j \rangle \tag{2.65b}$$

$$\mathbf{R} = \langle R[V_i], V_j \rangle \tag{2.65c}$$

$$i, j = 1, 2, 3, ...N \tag{2.65d}$$

As N is increased, the accuracy of the approximation increases, but the computations can become costly. The polynomial eigenvalue problem (2.64) is solved using the MATLAB function "polyeig." The solution produces eigenvalue, eigenvector pairs (λ,**c**), which correspond to different vibrational modes. For each mode λ is the dimensionless natural frequency and the vector **c** contains the coefficients that define the shape of the surface disturbance according to (4.78). In this research $N = 30$ terms are used for calculations. This strikes a balance between accuracy and computational costs, giving a relative eigenvalue convergence of 0.01% (see[85]).

2.3 Forced solution

The forced solution is when the forcing term in the operator equation (2.48) is not zero (i.e. $\hat{p}_d \neq 0$). Physically, this corresponds to the cylinder being oscillated in the vertical direction at a known frequency ω and amplitude P_d. The forced solution is more simple than the free solution because the frequency is no longer an unknown, it is a set input parameter. The operator equation for the forced case is

$$\lambda^2 M[y] + \lambda L[y; Oh] + R[y; Ec, Bo] = \hat{p}_d. \tag{2.66}$$

However, since the dimensionless frequency λ is known, the operator equation (2.66) can be simplified to

$$K[y; Oh, Ec, Bo] = \hat{p}_d, \tag{2.67}$$

where

$$K[y; Oh, \xi, Bo] = \lambda^2 M[y] + \lambda L[y; Oh] + R[y; Ec, Bo]. \tag{2.68}$$

This simplified operator equation (2.67) can be transformed into a matrix equation and then simply solved as a linear equation. Using the Rayleigh-Ritz method and the pinned basis functions basis functions, (2.67) is transformed into a matrix equation as follows:

$$\langle K[y_i], V_j \rangle = \langle \hat{p}_d, V_j \rangle \tag{2.69a}$$

$$\Rightarrow c_i \langle K[V_i], V_j \rangle = \langle \hat{p}_d, V_j \rangle \tag{2.69b}$$

Thus, the operator equation (2.67) is transformed into the matrix equation

$$\mathbf{Kc} = \mathbf{p}, \tag{2.70}$$

where

$$\mathbf{K} = \langle K[V_i], V_j \rangle \tag{2.71a}$$

$$\mathbf{p} = \hat{p}_d \langle 1, V_j \rangle \tag{2.71b}$$

$$i, j = 1, 2, 3, ...N \tag{2.71c}$$

Solving for the coefficient vector $\mathbf{c}$ is a simple linear operation:

$$\mathbf{c} = \mathbf{pK}^{-1} \tag{2.72}$$

As with the free disturbance, the vector $\mathbf{c}$ contains the coefficients that describe the surface disturbance according to (2.37). Again, N=30 terms are used in the matrix expansion. For a given m, the amplitude response can be computed over a range of frequencies, with spikes in the amplitude corresponding to vibrational modes ($n = 1$, $n = 2$, $n = 3$, etc.).

Chapter 3

Results and Experimental Comparison

In this chapter, results from the theoretical model are presented, and the impact of the dimensionless parameters (h, Bo, Oh, Ec) on the mode frequencies is explored. The validity of the model is demonstrated through extensive comparison to experimental data with various parameter values and boundary conditions.

3.1 Theoretical Results

3.1.1 Mode Shapes

A 3D rendering of several vibrational mode shapes that are explored in this research is shown in Figure 3.1. Note that these modes have a pinned contact condition around the rim of the cylinder. The modes are defined by both a radial mode number n and an azimuthal mode number m. The mode number indicates the number of nodes, or the number of times the wave crosses the undisturbed free surface of the fluid. A mode is designated by an (n, m) number pair, indicating both the radial and azimuthal mode numbers. For example, Figure 3.1a shows the shape of the (1,0) mode, which indicates $n = 1$ and $m = 0$ for this mode. Note that m can be 0,1,2,3, etc., but n cannot be zero, so it equals 1,2,3, etc. This is because a (0,0) mode would be a completely flat, undisturbed surface (the natural state of the system under consideration).

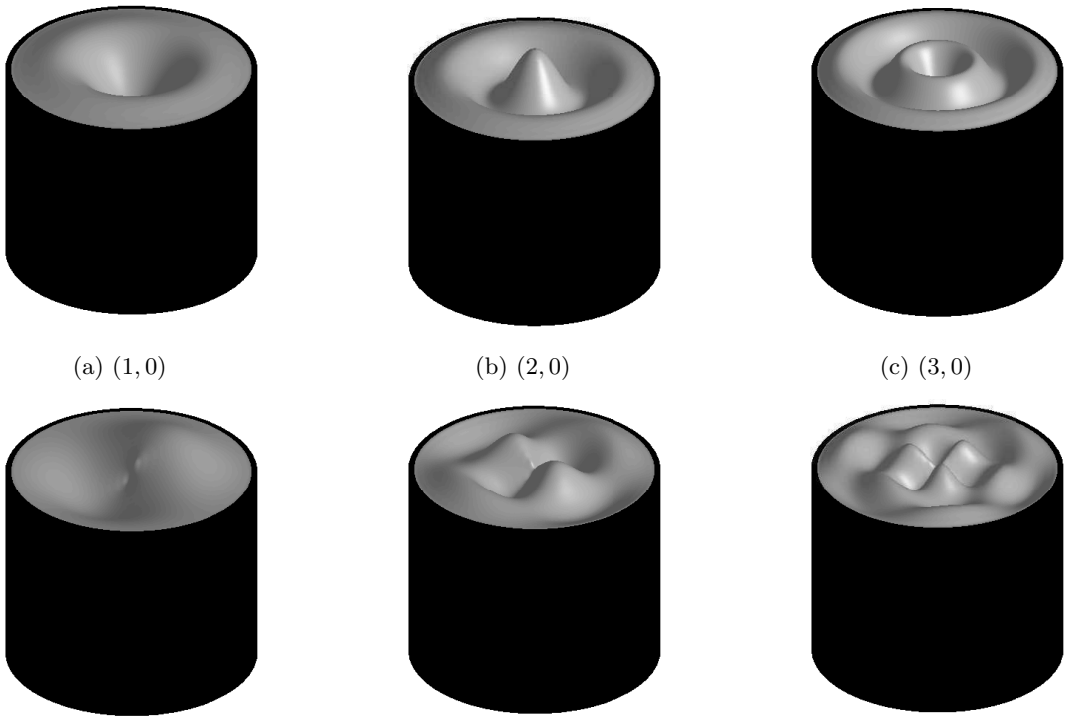

(a) $(1, 0)$ (b) $(2, 0)$ (c) $(3, 0)$

(d) $(1, 1)$ (e) $(2, 2)$ (f) $(3, 3)$

Figure 3.1: Illustration of various modes. (a)-(c) show the first three axisymmetric modes where $n = 1, 2, 3$, while (d)-(f) show modes with azimuthal waves where $m = 1, 2, 3$.

	$n=1$	2	3	4	5	6
$m=0$	28.50	42.15	56.76	73.12	91.35	111.39
1	19.82	35.07	49.10	64.58	81.89	101.05
2	26.41	41.20	56.04	72.49	90.78	110.85
3	32.10	47.29	63.09	80.56	99.82	120.81
4	37.49	53.46	70.31	88.81	109.03	130.91
5	42.83	59.78	77.71	97.23	118.40	141.17
6	48.23	66.28	85.30	105.84	127.95	151.59

Table 3.1: Pinned condition dimensionless natural frequencies for various modes. Calculations are for water in an infinite depth cylinder ($h=\infty$, $Bo=167$, $Oh=6\times10^{-4}$).

	$n=1$	2	3	4	5	6
$m=0$	26.43	39.00	52.52	67.81	85.02	104.09
1	17.74	32.33	45.31	59.72	75.99	94.16
2	23.25	37.76	51.59	67.02	84.31	103.44
3	27.90	43.11	57.98	74.48	92.79	112.87
4	32.27	48.53	64.54	82.12	101.44	122.46
5	36.60	54.11	71.28	89.95	110.27	132.20
6	40.98	59.86	78.22	97.97	119.27	142.10

Table 3.2: Sliding condition dimensionless natural frequencies for various modes. Calculations are for water in an infinite depth cylinder ($h=\infty$, $Bo=167$, $Oh=6\times10^{-4}$).

In Figure 3.1, (a)-(c) are axisymmetric modes, meaning that $m=0$. The shapes look something like ripples and are completely symmetric about the vertical axis. (d)-(f) in Figure 3.1 are non-axisymmetric modes, where $m\neq0$. The inclusion of azimuthal waves results in more complex modes shapes and more involved analysis.

3.1.2 Mode Frequencies

The first several natural frequencies are calculated for the pinned contact line condition and are shown in Table 3.1. These calculations are for water ($\sigma=71.7$ mN/m, $\mu=0.96$ mPa·s, $\rho=1000$ kg/m^3) in an infinite depth cylinder with a radius of $a=35$ mm. For comparison, the sliding contact line frequencies are also calculated and shown in Table 3.2.

For each azimuthal mode number m, the frequency increases as n increases. The converse is true with the exception of $m=0$. For $m\neq0$, as m increases for a given n, the frequency also increases. The $m=0$ frequencies fall in between $m=2$ and $m=3$. As can be seen in the tables, the first few frequencies in order are $(1,1)$, $(1,2)$, $(1,0)$, $(1,3)$, $(2,1)$, and so on. For all modes,

the pinned frequencies are higher than the sliding frequencies. Note that the difference between the pinned and sliding frequencies increases as both m and n increase.

3.1.3 Pressure and Velocity Fields

Figure 3.2 shows an example of the shape of three modes from a side view, along with the corresponding pressure and velocity fields. The first three axisymmetric modes are shown. Figures 3.2a-3.2c give a clear illustration of how n is related to the number of times the wave crosses the undisturbed free surface. The system is considered in polar coordinates, where the center of the cylinder is the origin and the r-direction radiates outward. Consequently, the radial mode number n corresponds to the number of times the wave crosses between the origin and the rim of the cylinder. For the (1,0) mode, the dashed line (representing the surface wave) crosses the solid line (representing the undisturbed free surface) a total of two times, but only once on each side as we travel from the center of the cylinder out to the rim. Likewise, the (2,0) mode crosses the undisturbed free surface twice on each side, the (3,0) mode crosses three times on each side, and so forth and so on.

Figures 3.2d-3.2f show the corresponding pressure fields in the cylinder for these three modes. Here yellow indicates regions of higher pressure, while blue denotes regions of lower pressure. For the (1,0) mode, the center is concave, which results in a higher pressure at the center of the cylinder and a lower pressure towards the cylinder walls. On the other hand, the (2,0) mode is convex, which creates a lower pressure region in the center of the cylinder and higher pressure moving outwards. Notice the two areas of particularly high pressure which correspond to the two concave regions. The pressure in the (3,0) mode varies as we move outward radially, corresponding to the convex and concave regions (the peaks and troughs of the surface waves), with the highest pressure in the center like the (1,0) mode.

Examples of the corresponding velocity fields are shown in Figures 3.2g-3.2i. In the (1,0), velocity field indicates fluid moving upwards towards the center of the cylinder, while in the (2,0) mode the fluid is moving downwards away from the center of the cylinder. The (3,0) mode again shows fluid moving upwards towards the center of the cylinder. This is because surface tension is acting as a restorative force, acting to restore the surface to an unperturbed state. The center of the (1,0) and (3,0) modes are concave, so surface tension is acting to "restore" the surface in an upward direction at this point. The (2,0) mode, on the other hand, is convex at the center, so surface tension is acting to "restore" the surface in a downward direction at the center.

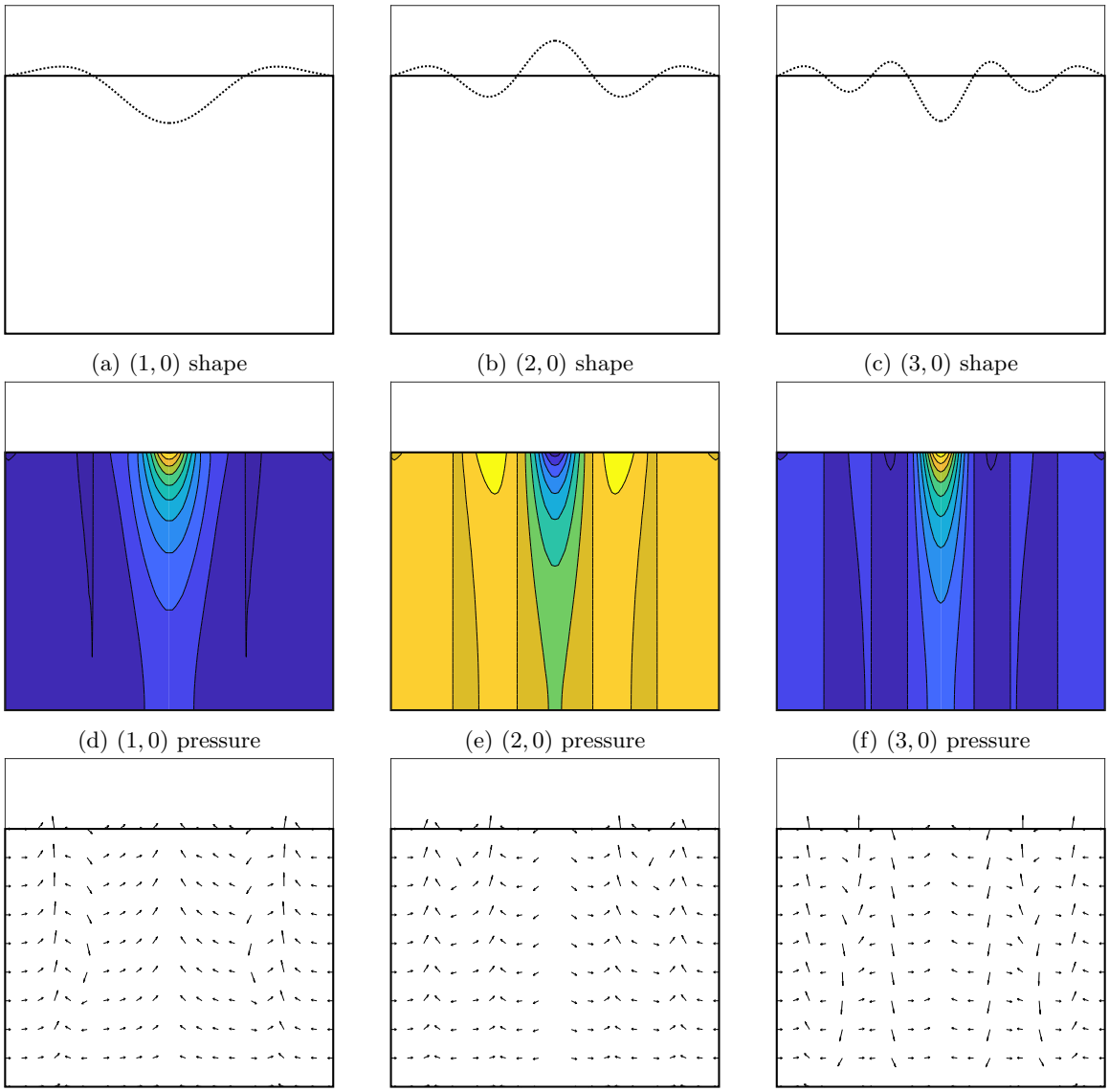

(a) $(1,0)$ shape (b) $(2,0)$ shape (c) $(3,0)$ shape

(d) $(1,0)$ pressure (e) $(2,0)$ pressure (f) $(3,0)$ pressure

(g) $(1,0)$ velocity (h) $(2,0)$ velocity (i) $(3,0)$ velocity

Figure 3.2: Illustration of the shape, pressure field, and velocity field of the first three axisymmetric modes (1,0), (2,0), and ((3,0). In (d)-(f), the light yellow indicates high pressure, while the dark blue indicates low pressure.

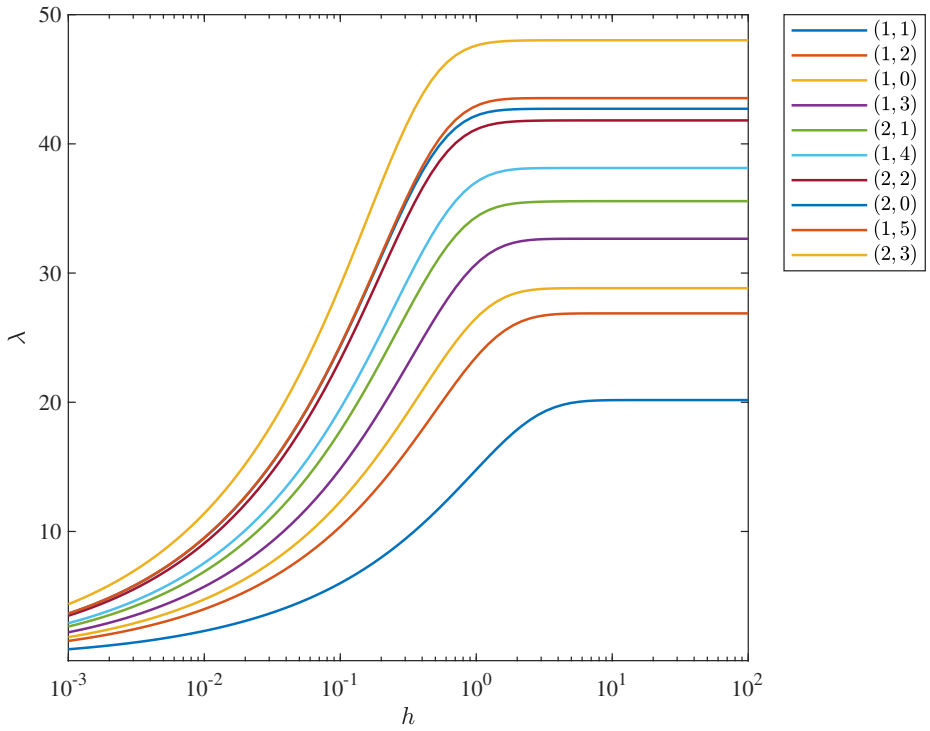

Figure 3.3: Semilog plot showing how the dimensionless frequency λ changes as the cylinder aspect ratio h varies ($Oh = 0$, $Ec = 0$, $Bo = 0$).

3.1.4 Free Response Parameter Variation

Varying the four dimensionless parameters Oh, Ec, Bo, and h affects the natural frequency of each mode. These effects are examined by varying each parameter individually while setting the others parameters equal to zero (Oh, Ec, and Bo) or infinity (h). This is done for the first ten modes. The results are shown in Figures 3.3 - 3.6.

3.1.4.1 Varying h

Figure 3.3 shows the effect of the aspect ratio h on the dimensionless frequency λ for the first ten modes. The semilog plot shows each curve initially steadily increasing and then reaching a clear transition point where each curve flattens out. The transition point represents the infinite depth limit, where the aspect ratio no longer affects the frequency, and occurs at about $h \sim 1$. Before this point, increasing the aspect ratio (which means increasing the depth relative to the radius) significantly increases the natural frequencies. Note that the infinite depth limit shifts to lower h values as the mode increases. Also note that the aspect ratio has a more significant effect on the

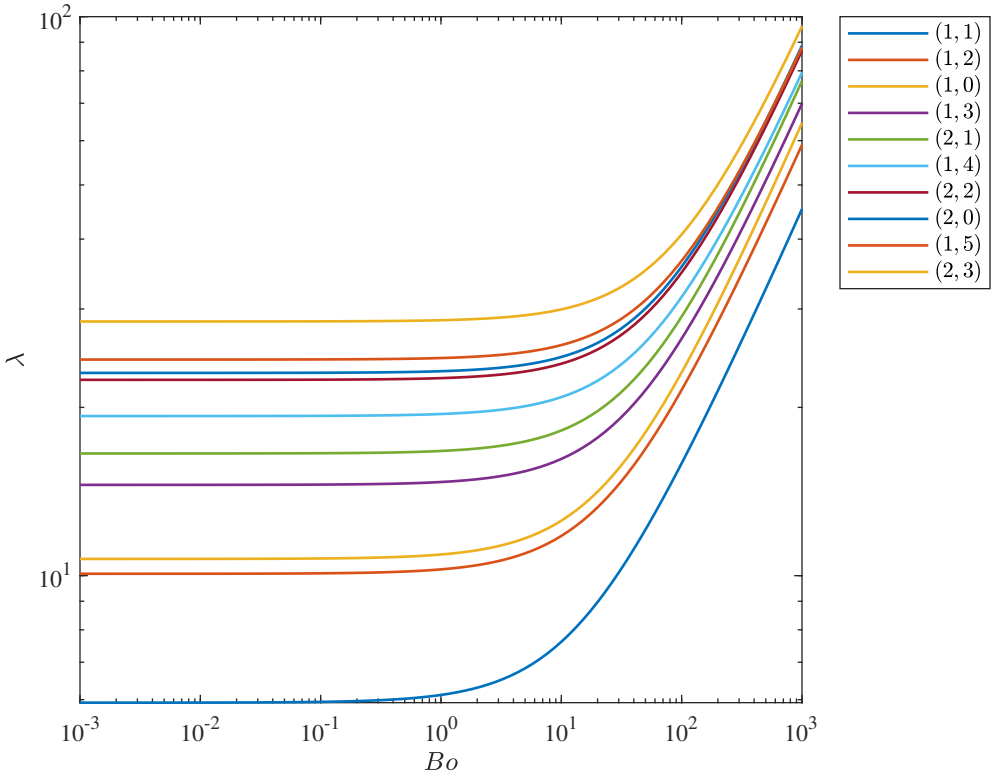

Figure 3.4: Semilog plot showing how the dimensionless frequency λ changes as the Bond number Bo varies ($h = \infty$, $Oh = 0$, $Ec = 0$).

frequency of higher modes, meaning that the slope of the curve is higher before it plateaus. The higher the mode, the more h will affect the frequency, but h will also stop affecting the frequency at a lower value.

3.1.4.2 Varying Bo

Figure 3.4 shows the effect of the Bond number on the natural frequency of the first ten modes. The log-log plot shows that the curves remain relatively flat until a transition point when they increase rapidly. This indicates that lower Bo values have no significant effect on the frequency, but after the transition point, the increasing the Bond number substantially increases the natural frequencies. The transition occurs around $Bo \sim 10$. At this point the waves transition from being pure capillary waves to being capillary-gravity waves. Notice that this transition point is not the same for all modes. It occurs at a higher Bo value for higher modes. Thus, as Bo is increased, gravity will affect the lower modes before the higher modes.

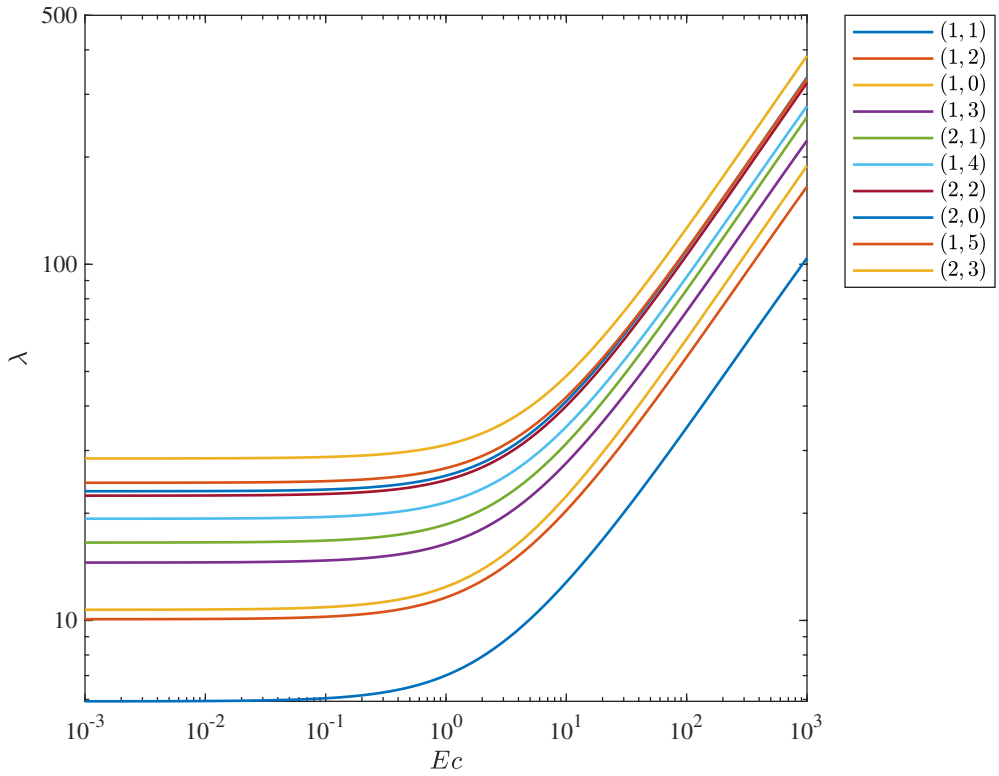

Figure 3.5: Semilog plot showing how the dimensionless frequency λ changes as the elastocapillary number Ec varies ($h = \infty$, $Oh = 0$, $Bo = 0$).

3.1.4.3 Varying Ec

In Figure 3.5, we see the effect of the elastocapillary number on the natural frequency of the first ten modes. The effect is similar to that of the Bond number in Figure 3.4. The curves remain relatively flat and then at a transition point begin to increase sharply. This indicates that low Ec values do not substantially affect the frequencies, but after the transition point, increasing the elastocapillary number significantly increases the natural frequency of each mode. This marks a transition from purely capillary waves to elasto-capillary waves, and this occurs around $Ec \sim 1$. Note that the transition Ec value increases as the modes increase. This is because higher modes have shorter wavelengths, which means that surface tension effects are more important than elastic effects.

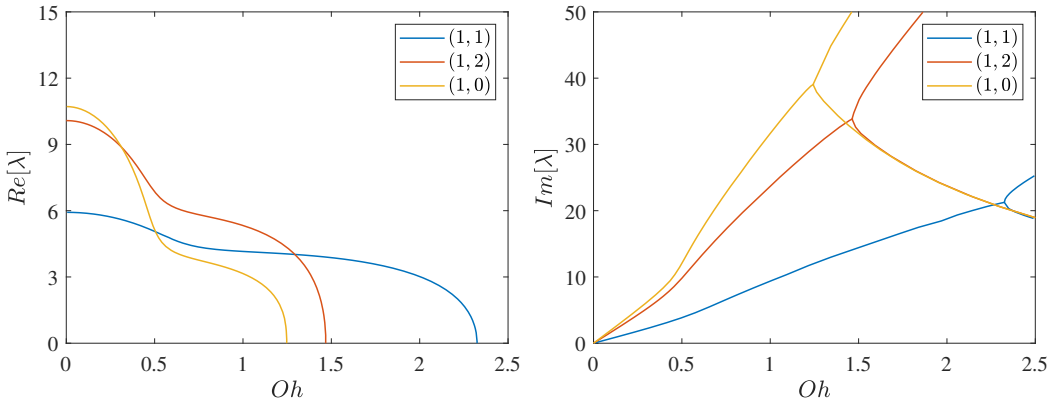

(a) Real frequency response

(b) Imaginary frequency response

Figure 3.6: Comparison of real and imaginary frequencies as the Ohnesorge number Oh is varied for the first three modes ($h = \infty$, $Ec = 0$, $Bo = 0$).

3.1.4.4 Varying Oh

Finally, Figure 3.6 shows how the natural frequency is affected by Oh for the first three modes. Unlike the first three parameters, the Onesorge number affects both the real and imaginary components of the frequency. The real component of the λ is shown in Figure 3.6a, while the imaginary component is shown in Figure 3.6b. $Re[\lambda]$ is the physical natural frequency, and $Im[\lambda]$ represents the viscous dissipation in the system.

In Figure 3.6a, we see that as the Oh increases, the frequency of each mode decreases until it becomes zero. This is because the Ohnesorge number is related to viscosity in the system. As Oh increases, the viscosity in the system, and therefore the viscous damping, increases until the system becomes overdamped, at which point the frequency become zero. This is clearly shown in Figure 3.6b, where we see that the imaginary frequency, which corresponds to viscous damping, starts at zero and increases as Oh increases. At a particular value of Oh, each mode undergoes a pitchfork bifurcation, which is the point at which the system becomes overdamped. It can be observed that the bifurcation points in Figure 3.6b precisely correspond with the zero frequency points in Figure 3.6a. The $(1,1)$ mode becomes overdamped at $Oh = 2.32$, the $(1,2)$ mode becomes overdamped at $Oh = 1.47$, and the $(1,0)$ mode becomes overdamped at $Oh = 1.25$.

Notice that the higher modes have higher natural frequencies at low Oh values. This makes sense - if the damping effects are low, the frequency should increase as the modes increase. However, as Oh increases, higher modes become overdamped before lower modes. Again, this makes sense

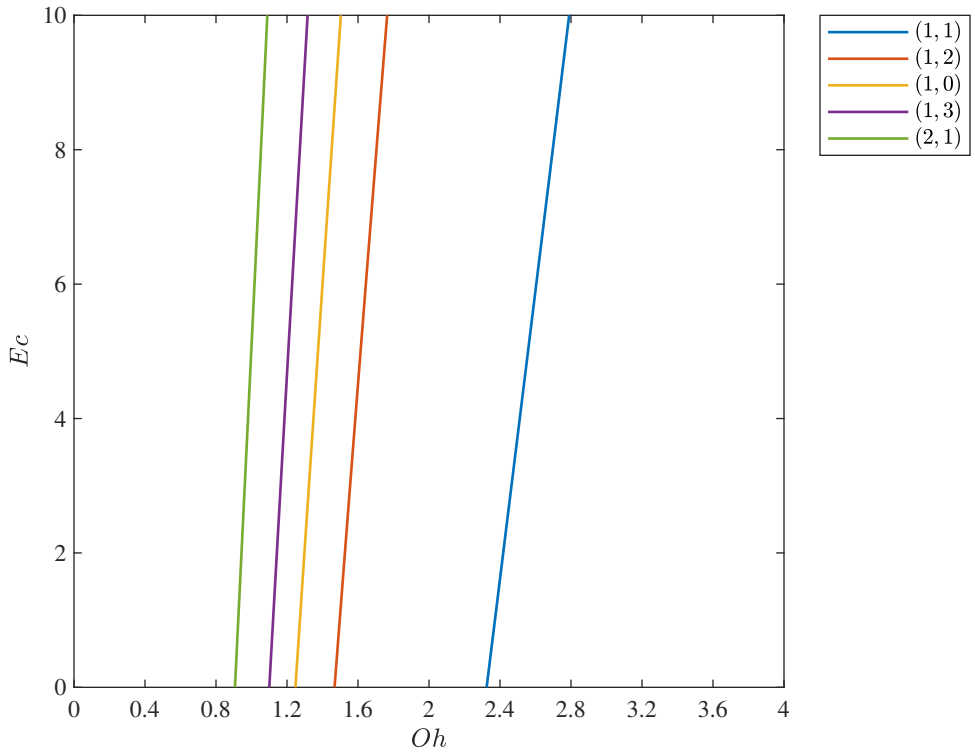

Figure 3.7: Curves representing the transition from underdamped to overdamped in relation to the elastocapillary number Ec and the Ohnesorge number Oh for the first five modes ($h = \infty$, $Bo = 0$).

because higher modes have higher frequencies, and therefore more oscillations, which means that greater motion will cause more dissipation. This results in the highest mode $(1, 0)$ being the first one to become overdamped, while the lowest mode $(1, 1)$ is the last one to become overdamped.

3.1.4.5 Critical Damping

In Figure 3.7, curves are plotted showing the dependence of the critical damping point on Oh and Ec. The curves represent the transition from underdamped to overdamped for the first five modes. As the mode increases, the curves shift to the left, which means that the critical Oh value decreases. This is expected based on Figures 3.6. For all three modes, as Ec increases, the critical Oh value shifts to the right, which means greater viscosity is required to damp out the oscillations. In addition, as the mode increases, the curves become steeper, which means that Ec has a less significant impact on the critical Oh value.

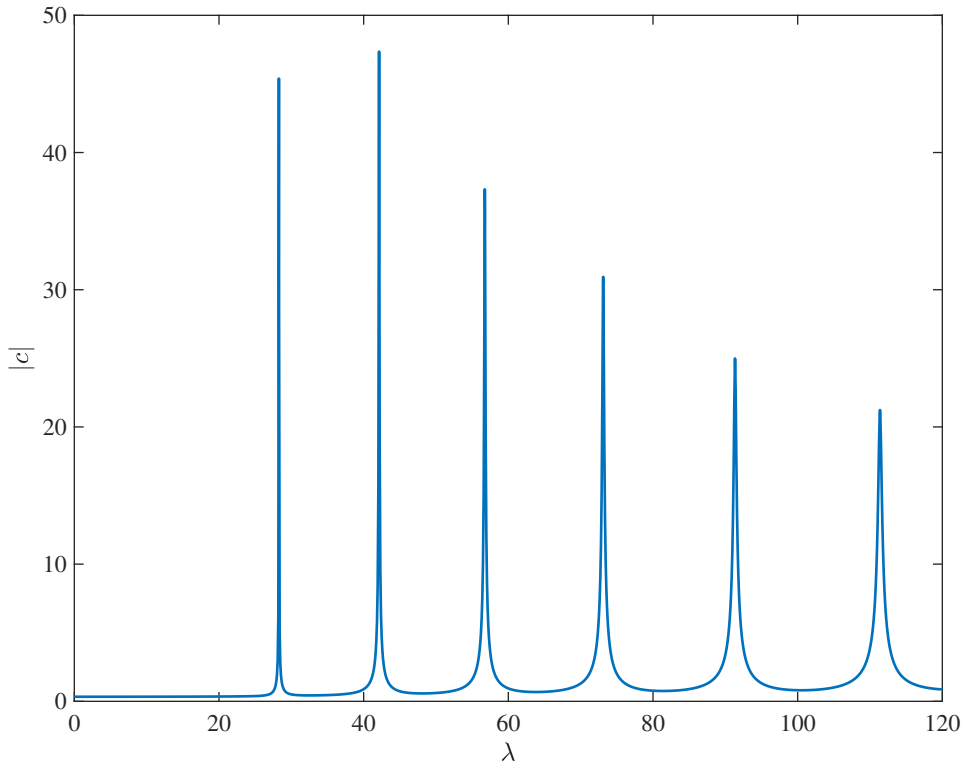

Figure 3.8: Forced amplitude response as the nondimensional frequency λ is increased for $m = 0$.

3.1.5 Forced Response Parameter Variation

In the forced case, we are imposing a given frequency and computing the amplitude response at that frequency. The amplitude is quantified by taking the norm of the coefficient vector $\mathbf{c}$, defined in equation 2.72. The coefficients are applied to the basis functions to give the shape of the mode. Thus, taking the norm gives a general indication of the magnitude of the wave amplitude of the mode.

An example is shown in Figure 3.8, where the norm of the coefficient vector is computed over a range of frequency values. The sharp peaks correspond to the natural or resonance frequencies, which are shown in Table 3.1. Note that this computation is for $m = 0$, and each peak is a corresponding n value. The first peak corresponds to $(1, 0)$, the second to $(2, 0)$, the third to $(3, 0)$, and so on. With the exception of the first peak, as n (and λ) increases, the amplitude decreases and the width of the peaks increases. The decreased amplitude and the increased width of the peaks corresponds to the viscous damping in the system, which we would expect to be larger at higher frequencies.

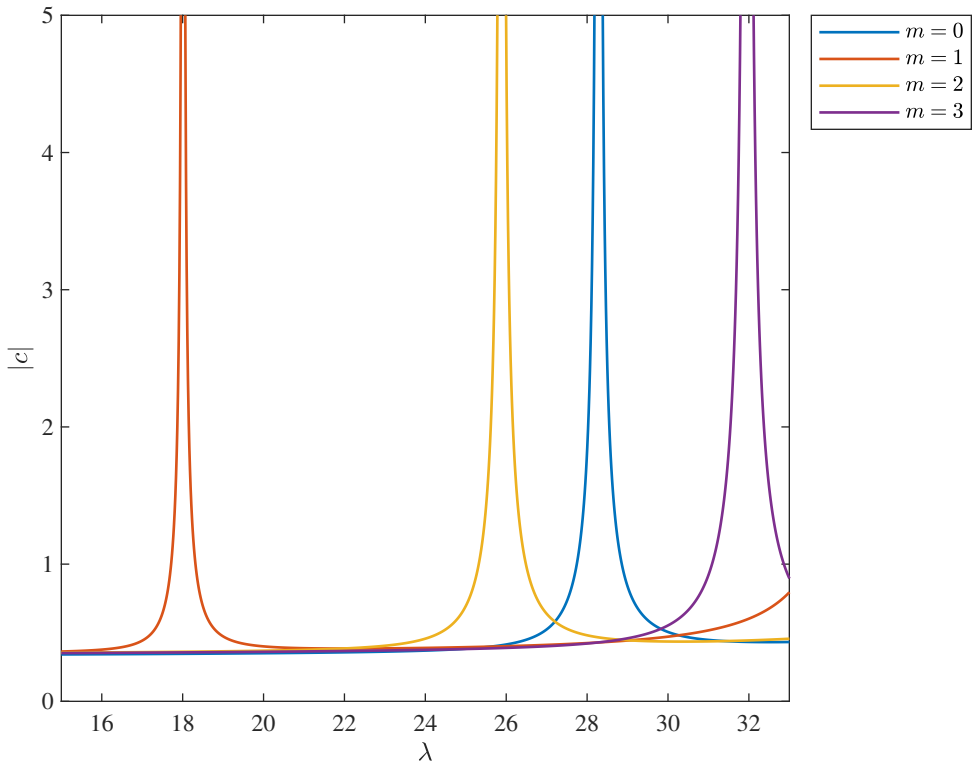

Figure 3.9: Comparison of the the first peak ($n = 1$) for several azimuthal modes.

Figure 3.9 shows the first peak (where $n = 1$) for several m values. For $m = 1 - 3$, as the azimuthal mode number increases, the peak frequency increases as well (i.e. the peaks shift to the right); however, $m = 0$ falls in between $m = 2$ and $m = 3$. This is precisely what we expect based on the frequency results in Table 3.1, where we see that the ascending order of these four modes is: $(1, 1)$, $(1, 2)$, $(1, 0)$, and $(1, 3)$.

3.1.5.1 Varying Oh

The effect of varying Oh and Ec is demonstrated for the forced cases, as with the free. Figure 3.10 shows the effect of changing the Ohnesorge number. As Oh increases, the peak flatten and spread out. Again, this is because Oh is related to viscous dissipation. Increased dissipation causes the modes to damp out, which we see in the reduced peaks. The peaks correspond to amplitude, so the smaller peaks indicate smaller amplitude waves. For the $(6, 0)$ mode (the peak on the far right), the highest Oh value almost completely damps out the amplitude, which physically means that this mode would be only just visible on the surface of the cylinder.

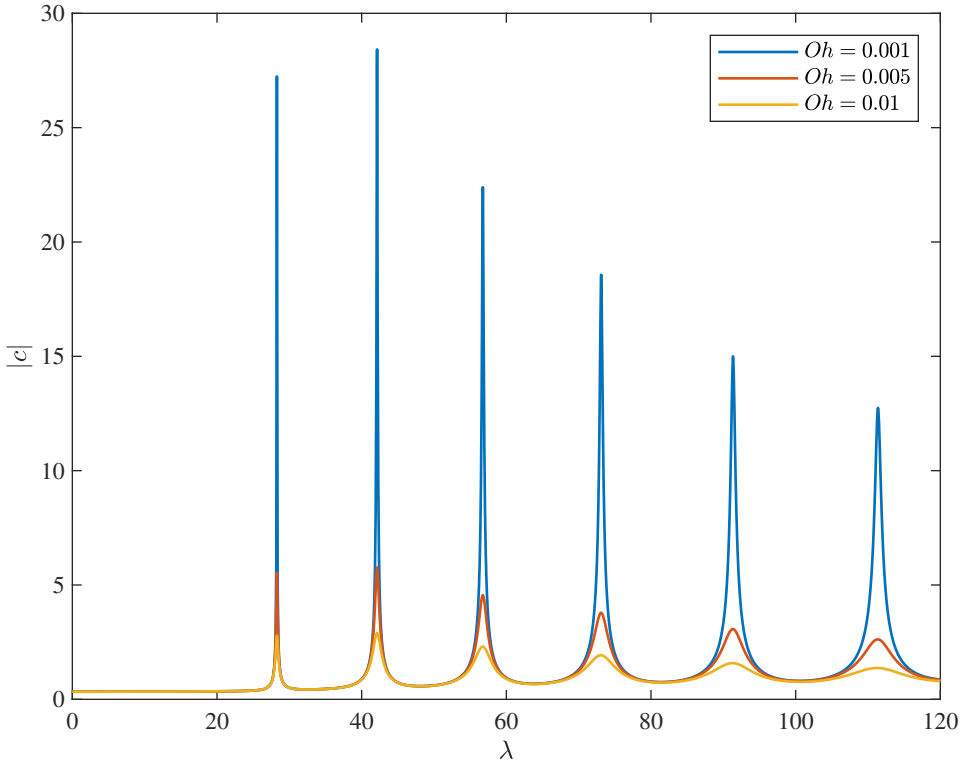

Figure 3.10: Example of how the forced response changes as the Ohnesorge number Oh is varied.

3.1.5.2 Varying Ec

Finally, Figure 3.11 shows the effect of changing the elastocapillary number. Several observations can be made. First, increasing Ec increases the natural frequencies (i.e. shifts all of the peaks to the right). This makes sense, because elasticity acts as a restoring force, which would tend to increase the frequency of oscillations. In addition, increasing Ec decreases the peak magnitude, which means that the wave amplitude is smaller. Again, this makes sense since elasticity acts a restoring force, which would tend to decrease the amplitude of the waves. Finally, we see that increasing Ec has a more substantial impact on the higher modes. Notice that, moving from right to left in Figure 3.11, the peaks become more spread out. This means that increasing Ec causes a larger frequency shift the higher the mode. For example, for $n = 1$, the peak frequency shifts from $\lambda = 28.6$ to $\lambda = 34.2$, an increase of 5.6. However, for $n = 2$, the peak frequency shifts from $\lambda = 42.8$ to $\lambda = 54.2$, an increase of 11.4. Figure 3.11 shows that this trend continues for higher modes as well.

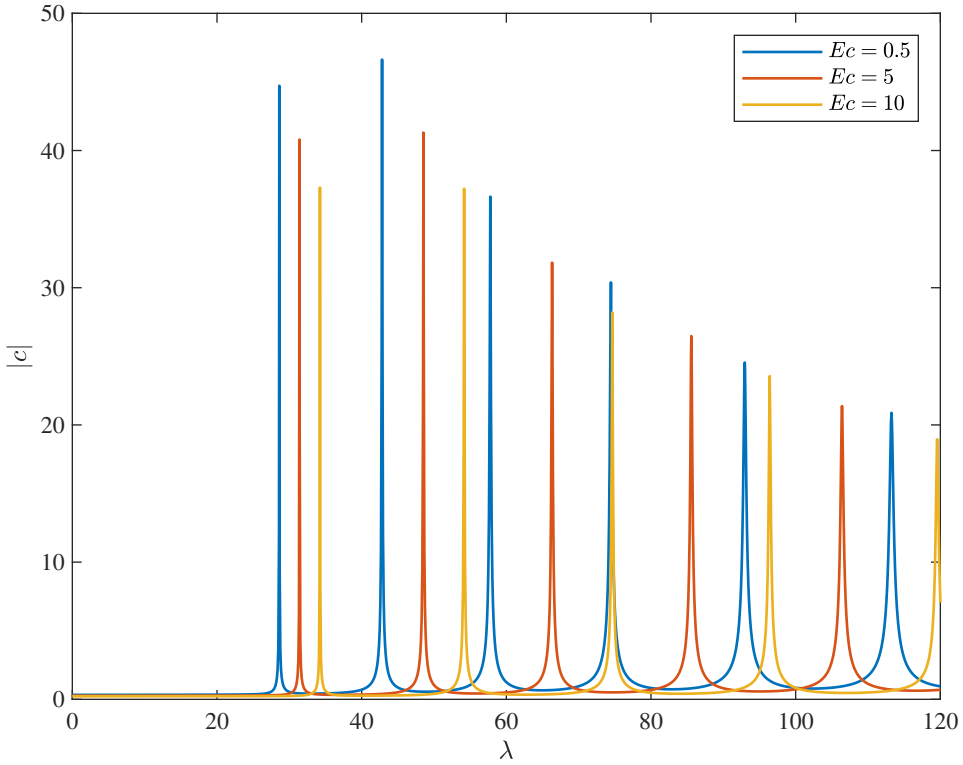

Figure 3.11: Example of how the forced response changes as the elastocapillary number Ec is varied.

3.2 Experimental Comparison

In order to verify the theoretical results, comparison was made with physical experiments corresponding to the theoretical system. These extensive experiments were performed by Dr. Xingchen Shao. In addition to thorough comparison of the mode frequencies of pure water, the theoretical results are compared to experiments with varying Ohnesorge numbers, elastocapillary numbers, aspect ratios, as well as experiments with both pinned and sliding contact line conditions. Comparing the theory with these experiments shows that the model which has been developed is accurate in a wide array of scenarios with different parameters.

In the experiments, surface waves were generated by placing a cylinder of fluid on an electromechanical shaker, which vibrates the cylinder in a vertical direction. With one exception, the cylinders were filled to the brim to created a pinned contact line condition, which is of primary interest for model comparison. One experiment compares sliding and pinned contact lines and is discussed below. A laser light system was used to detect and record Faraday waves on the fluid surface. A beam of collimated light was directed at the surface of the fluid, and the reflected

light was captured by a digital camera. In this way images were recorded of various modes and the corresponding driving frequencies. Importantly, the Faraday waves excited were subharmonic, meaning that the observed wave frequency was half of the driving frequency in the experiments. Thus, for comparison to the theoretical computations, the observed driving frequency for each mode was divided in half.

3.2.1 Shape

The orientation of the camera and light source was such that in the recorded images areas with a zero wave slope appear brighter, while areas with a non-zero wave slope appear to be darker. The result is essentially a wave slope magnitude image. Corresponding plots were created from the theoretical results, which are shown in Figure 3.12. This was accomplished by computing the absolute value of the magnitude of the gradient at each point and plotting it using an inverse color scheme (i.e. where the gradient is zero appears lightest, and where the gradient is largest appears darkest).

In Figure 3.12, (a)-(c) show the shapes of the first three axisymmetric modes, Below, (d)-(f) show the corresponding wave slope countour images, which are viewed from above the cylinder. The radial mode number n corresponds to the number of white rings that appear in the contour image. One can see that the (1,0) mode has one ring, the (2,0) mode has two rings, and the (3,0) mode has three rings. Naturally this is true for higher modes as well. Figures 3.12g-3.12l show examples that include azimuthal waves. In the wave slope image, the azimuthal mode number m corresponds to the number of radial white rays emanating from the origin divided by two. For a given mode number m, one will visually observe $2m$ white rays. In Figure 3.12, the (3,1) mode has two rays, the (3,2) mode has four rays, the (3,3) mode has size rays, and this pattern continues for higher azimuthal mode numbers.

Experimental images were obtained for the first fifty modes of water, corresponding to the mode frequencies shown in Table 3.3. The theoretical wave slope images correspond very well to the experimental images, which indicates that the mode shapes computed from the theoretical model are accurate.

(a) $(1, 0)$ shape

(b) $(2, 0)$ shape

(c) $(3, 0)$ shape

(d) $(1, 0)$ contour

(e) $(2, 0)$ contour

(f) $(3, 0)$ contour

(g) $(3, 1)$ shape

(h) $(3, 2)$ shape

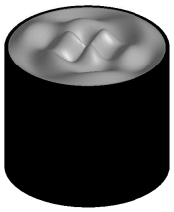

(i) $(3, 3)$ shape

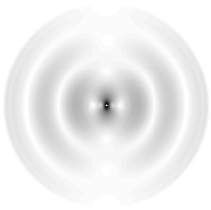

(j) $(3, 1)$ contour

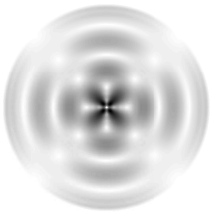

(k) $(3, 2)$ contour

(l) $(3, 3)$ contour

Figure 3.12: Illustration of the shape and corresponding wave slope contour image for various modes. (a)-(f) show the first three axisymmetric modes where $n = 1, 2, 3$, while (g)-(l) show modes with azimuthal waves where $m = 1, 2, 3$.

	$n=1$	2	3	4	5	6
$m=0$	5.82(0.4%)	8.67(0.3%)	11.68(0.2%)	15.05(1.0%)	18.80(1.1%)	22.92(0.8%)
1	3.71(0.2%)	7.20(0.0%)	10.10(0.0%)	13.29(0.1%)	16.85(0.3%)	20.79(0.5%)
2	5.33(0.5%)	8.47(0.3%)	11.53(0.3%)	14.92(0.1%)	18.68(0.6%)	22.81(0.8%)
3	6.58(0.4%)	9.73(0.7%)	12.98(0.1%)	16.58(0.7%)	20.54(0.3%)	
4	7.71(0.1%)	11.00(0.0%)	14.47(0.5%)	18.28(0.4%)		
5	8.81(1.0%)	12.30(0.8%)	15.99(0.7%)	20.01(0.9%)		
6	9.93(0.3%)	13.64(1.0%)	17.56(0.8%)	21.78(0.5%)		
7	11.06(1.2%)	15.02(0.5%)	19.16(0.2%)			
8	12.23(0.6%)	16.43(0.4%)				
9	13.43(0.3%)	17.89(3.9%)				
10	14.68(0.8%)	19.39(2.6%)				
11	15.96(0.3%)	20.92(1.3%)				
12	17.28(0.1%)					
13	18.64(0.3%)					
14	20.04(0.7%)					
15	21.49(0.1%)					

Table 3.3: Pinned condition dimensionless natural frequencies of various modes for water with $h = 0.629$.

3.2.2 Water Mode Frequency Comparison

The first 50 modes are computed for water (σ = 71.7 mN/m, μ = 0.96 mPa·s, ρ = 1000 kg/m^3) with a pinned contact line condition. The cylinder here has a depth $L = 22$ mm and a radius $a = 35$ mm, giving an aspect ratio of $h = 0.629$. Table 3.3 shows the results from the theoretical model compared with the experimental results. The percent difference from the experimentally recorded values is shown in parenthesis to the right of each mode frequency. Table 3.3 shows excellent agreement between the theoretical and experimental mode frequencies, with an average difference of 0.6%. All but four of the theoretical frequency values are within 1% difference of the experimental values; the four exceptions are the (1,7), (2,9), (2,10), and (5,0) modes. The largest difference is seen in the (2,9) mode at 3.9%. This difference is likely due to some experimental error. Despite a few larger differences, the agreement between the theory and experiment is excellent and demonstrates that the theoretical model which has been developed is reliable and valuable for predicting mode frequencies.

ratio	$Oh \times 10^3$	$n = 1$	2	3	4	5	6
0:1	0.60	5.82(0.4%)	8.67(1.5%)	11.68(2.4%)	15.05(4.4%)	18.80(4.3%)	22.92(5.0%)
1:5	0.94	5.79(1.6%)	8.59(2.2%)	11.51(4.6%)	14.77(4.7%)	18.40(6.8%)	22.39(6.9%)
1:3	1.30	5.78(1.4%)	8.55(1.7%)	11.43(4.8%)	14.64(7.4%)	18.21(7.5%)	22.13(10.1%)
1:2	1.85	5.77(1.1%)	8.51(2.5%)	11.35(5.9%)	14.51(7.2%)	18.02(8.2%)	21.87(9.9%)
2:3	2.70	5.75(0.9%)	8.47(2.1%)	11.28(6.2%)	14.39(7.9%)	17.85(10.3%)	21.64(10.9%)
3:1	29.43	5.71(2.0%)	8.35(4.3%)	11.03(5.8%)	13.96(7.1%)	OD	OD

Table 3.4: Pinned condition dimensionless natural frequencies of various modes for different glycerol/water ratios with $h = 0.629$.

3.3 Viscous Variation Comparison

While computing mode frequencies for water is a valuable baseline for validating the model, various parameter values are of particular interest as well. Table 3.4 shows theoretical computations for various Ohnesorge numbers, again in a cylinder with $h = 0.629$. Note that these are all axisymmetric modes, with $m = 0$. Experimentally, different Ohnesorge numbers were achieved by creating mixtures of glycerol and water at different ratios. In Table 3.4, the glycerol/water ratio is shown in the leftmost column. For example, the first row is a ration of 0:1, which is just pure water. The amount of glycerol increases as we move down the column, and as the ratio increases, so does the Ohnesorge number, which is shown in the second column. Once again, the percent difference between the theoretical frequencies (the values shown) and the experimentally observed frequencies is shown in parenthesis to the right of the values. Two of the modes were not experimentally observed and are noted as overdamped (OD). While not as close as the pure water values, there is still reasonable agreement between the theory and experiment. The average difference is 8.0%, with the smallest difference at 0.4% and the largest at 10.9%. Notice that the percent difference tends to increase both as the Ohnesorge number increases and as the mode number n increases. The former difference could be because of uncertainty in the material properties of the glycerol/water mixture. Small changes in the surface tension and density (along with the viscosity of course), have a significant impact on the computed results, so experimental error in measuring these two parameters could be resulting in larger differences for fluids with a higher glycerol/water ratio. It is uncertain why the percent difference increases as the mode number increases, as this effect is not observed for the pure water computations in Table 3.3.

G(Pa)	Ec	$n = 1$	2	3
1.2	0.59	5.90(1.7%)	8.84(3.9%)	11.93(9.0%)
3.6	1.76	6.06(0.9%)	9.16(2.6%)	12.41(0.1%)
8.4	4.10	6.35(0.7%)	9.77(2.4%)	13.32(6.4%)
15.3	7.47	6.76(3.9%)	10.58(6.6%)	14.52(1.5%)
20.2	9.82	7.03(3.3%)	11.12(5.7%)	15.32(6.9%)

Table 3.5: Pinned condition dimensionless natural frequencies of various modes for different agarose gels with $h = 0.629$.

3.4 Elastic Variation Comparison

Experimentally, agarose gels were used to observe modes with varying elasticity. Once again, these observations are for an aspect ratio of $h = 0.629$ and for axisymmetric modes with $m = 0$. The gels are modeled as having the density and surface tension of water and zero viscosity ($\sigma = 71.7$ mN/m, $\rho = 1000$ kg/m^3); the only parameter that changes is the shear modulus. The first three mode frequencies are computed for five different gels, and the results are shown in Table 3.5. The leftmost column indicates the shear modulus, and the corresponding elastocapillary number is shown in the second column. Again, theoretical frequencies are shown with the percent difference from the experimentally observed values shown in parenthesis to the right. The average difference is 3.7%, showing very good agreement between the theory and experiment.

3.5 Height Variation Comparison

Table 3.6 and Table 3.7 show results comparing cylinders with different aspect ratios. Table 3.6 shows frequencies for a cylinder with a radius a of 35 mm and a depth L of 22 mm, giving an aspect ratio of $h = 0.629$. Table 3.7 shows results for a cylinder with the same radius, but a depth of just 7 mm, giving an aspect ratio of $h = 0.2$. Results are computed for five different modes and four different Ohnesorge numbers. As before, the Ohnesorge number variation was experimentally achieved by using mixtures of glycerol and water for the fluid. Again, the glycerol to water ratio is shown in the leftmost column, with the corresponding Ohnesorge number shown in the second column. The percent differences between the displayed theoretical results and the experimentally observed values are shown in parenthesis to the right of each mode frequency. The agreement between the theory and experiment is excellent, with an average difference of 1.1% for the results in Table

Ratio	$Oh \times 10^3$	$(1,2)$	$(1,0)$	$(1,3)$	$(2,1)$	$(1,4)$
0:1	0.57	5.33(0.6%)	5.82(0.4%)	6.58(0.3%)	7.21(0.1%)	7.72(0.2%)
1:2	1.86	5.27(1.3%)	5.76(0.7%)	6.48(1.2%)	7.09(0.1%)	7.57(0.9%)
1:1	4.21	5.23(1.6%)	5.73(0.4%)	6.43(2.8%)	7.04(0.2%)	7.49(1.9%)
2:1	12.71	5.21(3.1%)	5.71(1.0%)	6.39(2.2%)	6.99(0.6%)	7.43(2.5%)

Table 3.6: Pinned condition dimensionless natural frequencies of various modes for different glycerol/water ratios with $h = 0.629$.

Ratio	$Oh \times 10^3$	$(1,2)$	$(1,0)$	$(1,3)$	$(2,1)$	$(1,4)$
0:1	0.57	4.07(0.8%)	4.75(1.1%)	5.55(0.9%)	6.43(0.4%)	6.93(0.5%)
1:2	1.86	4.02(1.9%)	4.70(0.0%)	5.47(0.5%)	6.34(1.0%)	6.81(1.3%)
1:1	4.21	3.99(2.4%)	4.67(0.6%)	5.42(0.4%)	6.28(0.3%)	6.74(0.6%)
2:1	12.71	3.98(4.6%)	4.66(1.2%)	5.40(3.7%)	6.25(0.9%)	6.70(1.5%)

Table 3.7: Pinned condition dimensionless natural frequencies of various modes for different glycerol/water ratios with $h = 0.2$.

	$(1,2)$	$(1,0)$	$(1,3)$	$(2,1)$
Sliding	3.49(0.3%)	4.29(2.2%)	4.66(0.9%)	5.72(2.1%)
Pinned	3.90(0.1%)	4.57(1.6%)	5.25(2.9%)	6.10(1.6%)

Table 3.8: Pinned and sliding dimensionless natural frequencies of various modes for a Triton/water solution with $h = 0.629$.

3.6 and an average difference of 1.2% for the results in Table 3.7. This comparison demonstrates the reliability of the model at different aspect ratios. From the experimental data, it is clear that changing the aspect ratio does not significantly impact the accuracy of the theoretical model.

3.6 Pinned vs. Sliding Comparison

While the theoretical analysis and experimentation has been largely concerned with the pinned contact line condition (as this is the more complicated case from a theoretical perspective), experiments were also performed to obtain sliding and pinned contact line results for the same modes. Experimentally, this was accomplished using a Triton/water solution of 0.0132g/300ml. This solution was modeled with a surface tension of $\sigma = 40.7$ mN/m. Four mode frequencies are computed and compared against the experimental values in Table 3.8. The theory and experiment show excellent agreement, with an average percent difference of 1.5%. The average difference for the

sliding case alone and the pinned case alone are 1.4% and 1.6%, respectively. This indicates that the results from the Rayleigh-Ritz methodology for the pinned condition are almost as accurate as the results from the simple dispersion relationship for the sliding condition.

Chapter 4

Rotational Theory

In the analysis outlined in Chapter 2, it is assumed that the flow is irrotational, as this greatly simplifies the analysis. In this chapter, a theoretical model is derived for axisymmetric surface waves on a viscoelastic fluid in an infinite depth cylinder where rotational flow in the fluid is included. The results are then compared to the irrotational model.

4.1 Derivation of governing equations

The problem definition sketch is shown in Figure 4.1. The setup is similar to the irrotational analysis, with several exceptions. First, to simplify the analysis, the cylinder is assumed to be of infinite depth. Second, rotation is allowed in the $r-z$ plane, but it is assumed that there is no swirl (i.e. there is no velocity in the θ direction). Finally, for simplicity, only axisymmetric modes are considered in this analysis (i.e. $m = 0$ only), which means that none of the variables are dependent on θ (e.g. $\eta(r, \theta, t) \rightarrow \eta(r, t)$). As for the irrotational analysis, the cylinder is filled to the brim with fluid, and the area above the fluid is filled with a passive gas that does not affect the system dynamics. A small perturbation $\eta(r, t)$ is applied to the free surface, allowing the height of the free surface, the fluid pressure, and the fluid velocity to be defined as base quantities of $O(1)$ and

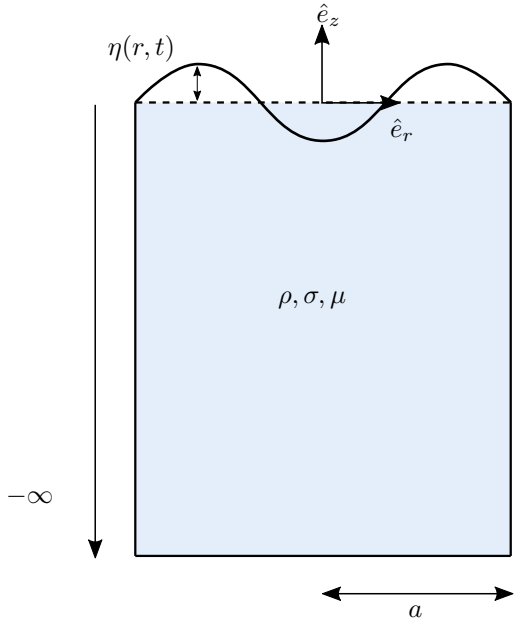

Figure 4.1: System definition sketch.

perturbed quantities of $O(\varepsilon)$:

$$z = 0 + \varepsilon\eta \tag{4.1a}$$

$$P = P_0 + \varepsilon P \tag{4.1b}$$

$$\mathbf{u} = \mathbf{u}_0 + \varepsilon\mathbf{u} \tag{4.1c}$$

Note that to simplify the calculations, the coordinate system origin is at the unperturbed free surface, whereas for the irrotational analysis it was located at the bottom surface of the cylinder. This means that the unperturbed free surface height is $z = 0$ instead of $z = L$. As before, the base pressure P_0 is equal to the pressure of the passive gas, and the base velocity $\mathbf{u}_0$ is equal to zero because the unperturbed fluid is assumed to be static. The vertical and radial lengths are nondimensionalized by the cylinder radius a:

$$r^* = \frac{r}{a} \rightarrow r = r^* a \tag{4.2a}$$

$$z^* = \frac{z}{a} \rightarrow z = z^* a \tag{4.2b}$$

For simplicity, we let r and z represent the dimensionless radius and height from here on. Thus, r varies from 0 to 1 and z varies from $-\infty$ to 0. The perturbation height η is kept in dimensional form for now.

4.1.1 Governing equations

For the irrotational analysis, the field equations governing the system were conservation of mass (continuity) and conservation of momentum (Navier-Stokes). These two equations are retained, but an additional governing equation is applied in the form of conservation of angular momentum (vorticity equation). For an incompressible fluid, the continuity equation is

$$\nabla \cdot \mathbf{u} = 0. \tag{4.3}$$

In the irrotational analysis, continuity was expressed as Laplace's equation, but because we do not assume irrotational flow here, the velocity cannot be defined in terms of a potential. The linearized incompressible Navier-Stokes equations can be expressed as

$$\rho \frac{\partial \mathbf{u}}{\partial t} = -\nabla P - \mu \nabla \times \nabla \times \mathbf{u}. \tag{4.4}$$

The linearization is explicitly shown in the derivation in Chapter 2. The vorticity is defined as the curl of the velocity:

$$\mathbf{\Omega} \equiv \nabla \times \mathbf{u} \tag{4.5}$$

Substituting this definition into (4.4) gives the vorticity equation:

$$\rho \frac{\partial \mathbf{\Omega}}{\partial t} = -\mu \nabla \times \nabla \times \mathbf{\Omega}, \tag{4.6}$$

Equations (4.3),(4.4), and (4.6) constitute the governing equations of the system. It is assumed that there is no swirl, meaning the azimuthal velocity (u_θ) is zero. Thus, the velocity field is defined as

$$\mathbf{u} = u_r(r, z, t)\hat{e}_r + u_z(r, z, t)\hat{e}_z, \tag{4.7}$$

and the vorticity is defined as

$$\mathbf{\Omega} = \Omega(r,z,t)\hat{e}_\theta = \left(\frac{\partial u_r}{\partial z} - \frac{\partial u_z}{\partial r}\right)\hat{e}_\theta. \tag{4.8}$$

4.1.2 Normal modes

The following normal modes are applied to separate the time dependency of the velocity, vorticity, pressure, and perturbation:

$$u_r(r,z,t) = v_r(r,z)e^{i\gamma t} \tag{4.9a}$$

$$u_z(r,z,t) = v_z(r,z)e^{i\gamma t} \tag{4.9b}$$

$$\Omega(r,z,t) = \omega(r,z)e^{i\gamma t} \tag{4.9c}$$

$$P(r,z,t) = p(r,z)e^{i\gamma t} \tag{4.9d}$$

$$\eta(r,t) = y(r)e^{i\gamma t} \tag{4.9e}$$

Note that unlike the irrotational analysis, there is not an azimuthal normal mode because we assume azimuthal symmetry (therefore there is no θ dependency). It should also be noted that γ is used in (4.9) for the dimensional frequency instead of ω because ω is used for the reduced vorticity. Substituting (4.9) into (4.3)-(4.6) results in the following reduced governing equations:

$$\nabla \cdot \mathbf{v} = 0 \tag{4.10a}$$

$$i\gamma\rho\mathbf{v} = -\nabla p - \mu\nabla \times \nabla \times \mathbf{v} \tag{4.10b}$$

$$i\gamma\rho\boldsymbol{\omega} = -\mu\nabla \times \nabla \times \boldsymbol{\omega} \tag{4.10c}$$

$$\boldsymbol{\omega} \equiv \nabla \times \mathbf{v} \tag{4.10d}$$

4.1.3 Boundary conditions

A no penetration condition is applied at the walls of the cylinder, requiring the radial fluid velocity to be zero at $r = 1$:

$$v_r = 0|_{r=1} \tag{4.11}$$

Three boundary conditions are applied at the free surface: a no shear condition, a kinematic condition, and a kinetic condition. The no shear condition requires that the shear in the fluid at the free surface be zero:

$$\frac{\partial v_r}{\partial z} + \frac{\partial v_z}{\partial r} = 0 \Big|_{z=0} \tag{4.12}$$

The kinematic condition requires that the fluid velocity be equal to the perturbation velocity at the free surface:

$$v_z = \frac{\partial \eta}{\partial t}\Big|_{z=0} \tag{4.13}$$

When normal modes are applied, (4.13) is reduced to

$$v_z = i\gamma y|_{z=0}. \tag{4.14}$$

Finally, a kinetic condition is applied to balance the normal stresses across the fluid/gas interface at the free surface. This is described by the Young-Laplace equation:

$$\hat{n} \cdot \underline{\underline{T}}^f \cdot \hat{n} - \hat{n} \cdot \underline{\underline{T}}^g \cdot \hat{n} = -\sigma(\nabla \cdot \hat{n}) \tag{4.15}$$

Here $\underline{\underline{T}}^f$ is the stress tensor in the fluid, $\underline{\underline{T}}^g$ is the stress tensor in the gas, σ is the surface tension at the interface, $\hat{n}$ is the unit normal vector of the surface (in the positive z direction). Since the normal stress for the gas is $-P_0$, the $O(\varepsilon)$ component is zero. We can thus express the $O(\varepsilon)$ component of (4.15) as

$$T_{zz} = \sigma(\nabla \cdot \hat{n})|_{z=0}. \tag{4.16}$$

For a Newtoniain fluid, the $O(\varepsilon)$ component of the normal stress in the z direction is

$$T_{zz} = -p + 2\mu\frac{\partial v_z}{\partial z}, \tag{4.17}$$

and the divergence of the surface normal vector is

$$\nabla \cdot \hat{n} = \frac{\sigma}{a^2}\left(\frac{d^2y}{dr^2} + \frac{1}{r}\frac{dy}{dr}\right). \tag{4.18}$$

The Young-Laplace equation, which describes the kinetic boundary condition, can then be written as

$$-p + 2\mu \frac{\partial v_z}{\partial z} = \frac{\sigma}{a^2} \left(\frac{d^2 y}{dr^2} + \frac{1}{r} \frac{dy}{dr} \right). \tag{4.19}$$

4.1.4 Velocity field decomposition

Using the Helmholtz decomposition theorem, the velocity field is decomposed into irrotational and rotational components [86]. The vorticity is thus defined in terms of a vector potential **B**:

$$\boldsymbol{\omega} = \nabla \times \mathbf{B} \tag{4.20}$$

Since the flow is axisymmetric, **B** must necessarily be in the z direction, and can therefore be written as follows [87]:

$$\mathbf{B} = B(r, z)\hat{e}_z. \tag{4.21}$$

The velocity can then be written in terms of a velocity potential (associated with the irrotational component of flow) and the vector potential (associated with the rotational component of flow):

$$\mathbf{v} = \mathbf{B} + \nabla \Psi \tag{4.22}$$

Thus, the velocity can be expressed as

$$\mathbf{v} = \left(\frac{\partial \Psi}{\partial r} \right) \hat{e}_r + \left(B + \frac{\partial \Psi}{\partial z} \right) \hat{e}_z. \tag{4.23}$$

Applying normal modes and separating variables, B and Ψ are defined as follows:

$$B(r, z, t) = T_n(z) J(k_n r) e^{i\gamma t} \tag{4.24a}$$

$$\Psi(r, z, t) = \phi_n(z) J(k_n r) e^{i\gamma t} \tag{4.24b}$$

$T_n(z)$ and $\phi_n(z)$ are unknown functions of z which will be solved for. For both B and Ψ, the r component is defined in terms of a series of Bessel functions of the form $J(k_n r)$. Here k_n is the nth zero of J', which satisfies the no penetration condition at the cylinder wall.

4.1.5 Vorticity equation

To find an equation for $T_n(z)$, $B(r,z,t)$ is substituted into the vorticity equation (4.10c). The vorticity is found by taking the curl of $\mathbf{B}$:

$$\boldsymbol{\omega} = \nabla \times \mathbf{B} = -\frac{\partial B}{\partial r}\hat{e}_\theta \tag{4.25}$$

The curl of the curl of $\boldsymbol{\omega}$ is calculated to be

$$\nabla \times \nabla \times \left(-\frac{\partial B}{\partial r}\right)\hat{e}_\theta = \frac{\partial}{\partial r}\left(\frac{\partial^2 B}{\partial z^2} + \frac{\partial^2 B}{\partial r^2} + \frac{1}{r}\frac{\partial B}{\partial r}\right). \tag{4.26}$$

Substituting (4.26) into (4.10c) gives

$$i\gamma\rho a^2\left(-\frac{\partial B}{\partial r}\right) = -\mu\frac{\partial}{\partial r}\left(\frac{\partial^2 B}{\partial z^2} + \frac{\partial^2 B}{\partial r^2} + \frac{1}{r}\frac{\partial B}{\partial r}\right), \tag{4.27}$$

which reduces to

$$i\gamma\rho a^2 B = \mu\left(\frac{\partial^2 B}{\partial z^2} + \frac{\partial^2 B}{\partial r^2} + \frac{1}{r}\frac{\partial B}{\partial r}\right). \tag{4.28}$$

Substituting in the definition of B (4.24a) into (4.28) and rearranging, the vorticity equation becomes

$$\left(\frac{\partial^2}{\partial z^2} + \frac{\partial^2}{\partial r^2} + \frac{1}{r}\frac{\partial}{\partial r}\right)T_n(z)J(k_n r) - \frac{i\gamma\rho a^2}{\mu}T_n(z)J(k_n r) = 0. \tag{4.29}$$

According to the Bessel equation, assuming azimuthal symmetry:

$$\left(\frac{\partial^2}{\partial r^2} + \frac{1}{r}\frac{\partial}{\partial r}\right)J(k_n r) = -k_n^2 J(k_n r) \tag{4.30}$$

Substituting (4.30) into (4.29), we have

$$\frac{\partial^2 T_n}{\partial z^2}J(k_n r) - k_n^2 T_n J(k_n r) - \frac{i\gamma\rho a^2}{\mu}T_n J(k_n r) = 0, \tag{4.31}$$

which reduces to

$$\frac{\partial^2 T_n}{\partial z^2} - \left(k_n^2 + \frac{i\gamma\rho a^2}{\mu}\right)T_n = 0. \tag{4.32}$$

4.1.6 Continuity equation

The devinition of $\mathbf{v}$ (4.22) is substituted into the continuity equation (4.10a) to find an equation for $\phi_n(z)$. The divergence of the velocity is

$$\nabla \cdot \left[\frac{\partial \Psi}{\partial r} \hat{e}_r + \left(B + \frac{\partial \Psi}{\partial z} \right) \hat{e}_z \right] = \frac{\partial^2 \Psi}{\partial r^2} + \frac{1}{r} \frac{\partial \Psi}{\partial r} + \frac{\partial^2 \Psi}{\partial z^2} + \frac{\partial B}{\partial z}. \tag{4.33}$$

Substituting the definition of Ψ (4.24b) into (4.33) gives

$$\left(\frac{\partial^2}{\partial r^2} + \frac{1}{r} \frac{\partial}{\partial r} + \frac{\partial^2}{\partial z^2} \right) \phi_n(z) J(k_n r) = -\frac{\partial}{\partial z} T_n(z) J(k_n r). \tag{4.34}$$

Using the Bessel equation correlation (4.30), the continuity equation can be simplified to

$$\frac{\partial^2 \phi_n}{\partial z^2} J(k_n r) - k_n^2 \phi_n J(k_n r) = -\frac{\partial T_n}{\partial z} J(k_n r), \tag{4.35}$$

which reduces to

$$\frac{\partial^2 \phi_n}{\partial z^2} - k_n^2 \phi_n = -\frac{\partial T_n}{\partial z}. \tag{4.36}$$

Equations (4.32) and (4.36) can be solved for T_n and ϕ_n.

4.1.7 Solution for T_n

Equation (4.32) can be rewritten as

$$T_n{}'' - \hat{k}^2 T_n = 0, \tag{4.37}$$

where

$$\hat{k}^2 = k^2 + \frac{i\gamma\rho a^2}{\mu}. \tag{4.38}$$

Note that the n subscript for k has been dropped for convenience. This is a simple homogeneous second order differential equation whose solution is of the form

$$T_n = c_1 e^{\hat{k}z} + c_2 e^{-\hat{k}z}. \tag{4.39}$$

Because the cylinder is of an infinite depth, $T_n \to 0$ as $z \to -\infty$, which implies that $c_2 = 0$. Thus, the solution to (4.37) can be written as

$$T_n = A_n e^{\hat{k}z}. \tag{4.40}$$

4.1.8 solution for ϕ_n

Equation (4.36) can be written as

$$\phi_n'' - k^2\phi_n = -T_n'. \tag{4.41}$$

Since this equation is not homogeneous, the method of undetermined coefficients is used to find a solution. The solution is separated into the homogeneous solution and the particular solution:

$$\phi_n = \phi_h + \phi_p \tag{4.42}$$

The homogeneous solution ϕ_h is the solution to

$$\phi_h'' - k^2\phi_h = 0. \tag{4.43}$$

As with equation (4.37), the solution is exponential. Since the cylinder is of an infinite depth, the solution is

$$\phi_h = B_n e^{kz}. \tag{4.44}$$

The particular solution is found to be

$$\phi_p = -\frac{A_n\hat{k}}{\hat{k}^2 - k^2}e^{\hat{k}z}. \tag{4.45}$$

The total solution can thus be written as

$$\phi_n = B_n e^{kz} - \frac{A_n\hat{k}}{\hat{k}^2 - k^2}e^{\hat{k}z}. \tag{4.46}$$

4.1.9 Boundary conditions

The shear boundary condition at the free surface is defined by equation (4.12). By substituting equation (4.24) into (4.23), the fluid velocity components can be written as

$$v_r = \phi_n J' \tag{4.47a}$$

$$v_z = T_n J + \phi_n' J \tag{4.47b}$$

Note that $J(k_n r)$ is denoted as J for simplicity. Plugging in the velocity components to the shear condition (4.12) results in

$$\phi_n' J' + T_n J' + \phi_n' J' = 0, \tag{4.48}$$

which can be simplified to

$$T_n + 2\phi_n' = 0. \tag{4.49}$$

The kinematic condition is defined by equation (4.14). Substituting in the definition of v_z (4.47b) gives

$$T_n J + \phi_n' J = i\gamma y. \tag{4.50}$$

Since the Bessel functions appear in the r component of the velocity solution, it is natural to define the surface disturbance y as a Bessel series:

$$y = \sum_{n=1}^{\infty} C_n J(k_n r) \tag{4.51}$$

Due to the orthogonality of the Bessel functions, C_n is necessarily defined as

$$C_n = \{y\} \equiv \frac{\langle y, J \rangle}{\langle J, J \rangle}, \tag{4.52}$$

where the inner product is defined as

$$\langle g(r), h(r) \rangle = \int r g(r) h(r) dr. \tag{4.53}$$

Substituting this definition of y into (4.50) gives

$$T_n J + \phi_n' J = i\gamma\{y\}J, \tag{4.54}$$

which can be reduced to

$$T_n + \phi_n' = i\gamma\{y\}. \tag{4.55}$$

Substituting in the solutions for T_n and ϕ_n into equation (4.49) and evaluating at $z = 0$ gives the shear condition in terms of the coefficients A and B:

$$A_n + 2B_n k - \frac{2A_n \hat{k}^2}{\hat{k}^2 - k^2} = 0 \tag{4.56}$$

Similarly, the solutions for T_n and ϕ_n are substituted into (4.55) and evaluated at $z = 0$ to give the kinematic condition in terms of A and B:

$$A_n + B_n k - \frac{A_n \hat{k}^2}{\hat{k}^2 - k^2} = i\gamma\{y\} \tag{4.57}$$

Solving equations (4.56) and (4.57) as a system of two equations and two unknowns gives solutions for A_n and B_n:

$$A_n = i\gamma 2\{y\} \tag{4.58a}$$

$$B_n = \frac{i\gamma\{y\}\left(\hat{k}^2 + k^2\right)}{k\left(\hat{k}^2 - k^2\right)} \tag{4.58b}$$

Substituting the solutions for A and B into equations (4.40) and (4.46), we can write the solutions to T_n and ϕ_n as

$$T_n = i\gamma 2\{y\}e^{\hat{k}z} \tag{4.59a}$$

$$\phi_n = \frac{i\gamma\{y\}\left(\hat{k}^2 + k^2\right)}{k\left(\hat{k}^2 - k^2\right)}e^{kz} - \frac{i\gamma 2\{y\}\hat{k}}{\hat{k}^2 - k^2}e^{\hat{k}z}. \tag{4.59b}$$

Recall that $T_n(z)$ is related to the rotational component of velocity, and $\phi_n(z)$ is related to the irrotational component of velocity.

4.1.10 Pressure

To define the pressure at the free surface, the solutions for T_n and ϕ_n are substituted into the reduced momentum balance equation (4.10b). The curl of the curl of the velocity in the r-direction is

$$\nabla \times \nabla \times \mathbf{v} = \left(-\frac{\partial^2 v_r}{\partial z^2} + \frac{\partial^2 v_z}{\partial z \partial r} \right) \hat{e}_r = \frac{\partial}{\partial r} \left(\frac{\partial B}{\partial z} \right) \hat{e}_r. \tag{4.60}$$

The momentum balance in the r-direction (4.10b) can then be written as

$$i\gamma\rho \frac{\partial \Psi}{\partial r} = -\frac{\partial p}{\partial r} - \mu \frac{\partial}{\partial r} \left(\frac{\partial B}{\partial z} \right), \tag{4.61}$$

which can be reduced to

$$i\gamma\rho\Psi = -p - \mu \frac{\partial B}{\partial z}. \tag{4.62}$$

Substituting the definitions of B and Ψ into (4.62) and solving for p, the pressure can be expressed as

$$p = \left(-i\gamma\rho\phi_n - \mu {T_n}' \right) J. \tag{4.63}$$

4.1.11 Young-Laplace equation

Substituting the definition of pressure (4.63) into the Young-Laplace equation (4.19) gives

$$-\left(-i\gamma\rho\phi_n - \mu {T'}_n \right) J + 2\mu \left(T' + {\phi''}_n \right) J = \frac{\sigma}{a^2} \left(\frac{d^2 y}{dr^2} + \frac{1}{r} \frac{dy}{dr} \right), \tag{4.64}$$

which can be simplified to

$$\left(2\mu {\phi''}_n + i\gamma\rho\phi_n + 3\mu {T'}_n + \rho g\{y\} \right) J = \frac{\sigma}{a^2} \left(\frac{d^2 y}{dr^2} + \frac{1}{r} \frac{dy}{dr} \right). \tag{4.65}$$

Equation (4.65) is an integro-differential in terms of the growth rate γ and the surface disturbance y. Substituting solutions for T_n and ϕ_n (4.59), along with the definition of $\hat{k}$ (4.38), into equation (4.65) produces an equation governing the dynamics of the system in terms of γ and y. After simplification,

the result is

$$\gamma^2\left(-\frac{\rho a\{y\}}{k}J\right)+i\gamma\left(\frac{4\mu k\{y\}}{a}J\right)+\mu^2\left(\frac{4k^3\{y\}}{\rho a^3}J\right) - \mu^2\left(\frac{4k^2\hat{k}\{y\}}{\rho a^3}J\right)=\frac{\sigma}{a^2}\left(\frac{d^2y}{dr^2}+\frac{1}{r}\frac{dy}{dr}\right). \quad (4.66)$$

Note that two of the terms on the left hand side of the equation are proportional to μ^2. If we assume a small viscosity, i.e. $\mu \ll 1$, then these two terms can be neglected and we have:

$$\gamma^2\left(\frac{\rho a\{y\}}{k}\right)-i\gamma\left(\frac{4\mu k\{y\}}{a}\right)+\frac{\sigma}{a^2}\left(\frac{d^2y}{dr^2}+\frac{1}{r}\frac{dy}{dr}\right)=0 \quad (4.67)$$

4.1.12 Non-dimensionalize

The surface perturbation y is now scaled by the cylinder radius such that

$$y^*=\frac{y}{a}\rightarrow y=y^*a. \quad (4.68)$$

For simplicity the asterisk is dropped from now on. Applying this scaling to (4.67) results in the following dimensionless equation:

$$\lambda^2\left(\frac{\{y\}}{k}J\right)-i\lambda\left(4\left(Oh\right)k\{y\}J\right)+\left(\frac{d^2y}{dr^2}+\frac{1}{r}\frac{dy}{dr}\right)=0 \quad (4.69)$$

Here λ is the dimensionless frequency and Oh is the Ohnesorge number:

$$\lambda\equiv\sqrt{\frac{\rho a^3\gamma^2}{\sigma}} \quad (4.70a)$$

$$Oh\equiv\frac{\mu}{\sqrt{\rho\sigma a}} \quad (4.70b)$$

$$(4.70c)$$

Note that k and J are summed for $n=1,2...\infty$. Applying summation notation, equation (4.69) is be written as

$$\lambda^2\sum_{n=1}^{\infty}\frac{\{y\}}{k_n}J_n-i\lambda4\left(Oh\right)\sum_{n=1}^{\infty}k_n\{y\}J_n+\left(\frac{d^2y}{dr^2}+\frac{1}{r}\frac{dy}{dr}\right)=0. \quad (4.71)$$

For simplicity, equation (4.69) is expressed as an operator equation:

$$\lambda^2 M[y] + \lambda L[y; Oh] + R[y] = 0, \tag{4.72}$$

The operator $M[y]$ represents the inertial term, defined as

$$M[y] \equiv \sum_{n=1}^{\infty} \frac{1}{k_n}\{y\} J_n(k_n r). \tag{4.73}$$

The operator $L[y; Oh]$ is the viscous damping term, defined as

$$L[y; Oh] \equiv i4\,(Oh) \sum_{n=1}^{\infty} k_n \{y\} J_n(k_n r). \tag{4.74}$$

The operator $R[y]$ is related to the curvature (surface energy) at the interface, and is defined as

$$R[y] = \frac{d^2 y}{dr^2} + \frac{1}{r}\frac{dy}{dr}. \tag{4.75}$$

Note that the result derived here is the same as for the irrotational analysis, except that the coefficient in the L operator is 4 instead of 2.

4.1.13 Basis functions

Previously, the surface disturbance was expressed as a series of Bessel functions; however, these functions do not satisfy the pinned edge condition around the rim of the cylinder ($r = a$, $z = 0$). In order to account for this, modified Bessel functions are computed, which are used as basis functions in the Rayleigh-Ritz method solution. The same method used in the irrotational analysis is used here, in which modified Bessel functions are defined as follows:

$$S_n(r) = J_n(k_n r) - \frac{J_n(k_n)}{J_n(k_1)} J_n(k_1 r) \qquad n = 2, 3, ...N \tag{4.76}$$

It can be easily seen that if $r = 1$, S_n must necessarily be zero, which creates the required pinned condition. However, S_1 is zero everywhere, so the function space is reduced to $N - 1$ and n begins counting from 2. In addition, the functions S_n are not orthogonal. The Grahm-Schmidt orthogonolization process is used to remedy this. The resulting orthogonal functions that satisfy the pinned

edge condition are denoted $V_n(r)$, where $n = 1, 2, 3, ...N$ These functions necessarily satisfy

$$\int_0^1 rV_i(r)V_j(r)dr \qquad i \neq j. \tag{4.77}$$

Thus the surface disturbance can be expressed as a linear combination of these modified basis functions:

$$y(r) = \sum_{n=1}^{\infty} c_n V_n(r) \tag{4.78}$$

4.1.14 Rayleigh-Ritz

Equation (4.71) is a polynomial eigenvalue problem, which is once again solved using the Rayleigh-Ritz method. Inner products are taken with the orthogonal basis functions to form the following matrix equation:

$$(\lambda^2\mathbf{M} + \lambda\mathbf{L} + \mathbf{R})\mathbf{c} = 0, \tag{4.79}$$

where the matrices are define as

$$\mathbf{M} = \langle M[V_i], V_j\rangle \tag{4.80a}$$

$$\mathbf{L} = \langle L[V_i], V_j\rangle \tag{4.80b}$$

$$\mathbf{R} = \langle R[V_i], V_j\rangle \tag{4.80c}$$

$$i, j = 1, 2, 3, ...N \tag{4.80d}$$

Again, solving (4.79) gives an approximate solution to the problem in the form of eigenvalue, eigenvector pairs $(\lambda, \mathbf{c})$, with the accuracy of the solution increasing as N is increased. Each $(\lambda, \mathbf{c})$ pair corresponds to a vibrational mode, λ being the natural frequency and $\mathbf{c}$ being a vector of coefficients which when applied to (4.78) give the shape of the surface perturbation (i.e. the shape of the mode). As for the irrotational computations, equation (4.79) is solved using the "polyeig" function in MATLAB.

4.2 Results and comparison

For water (σ = 71.7 mN/m, μ = 0.96 mPa·s, ρ = 1000 kg/m^3), the eigenvalues are computed for the first six axisymmetric modes and shown in Table 4.1. Note that since these are

Mode	Re[λ_r]	Im[λ_r]	Re[λ_i]	Im[λ_i]
1	10.35	0.020	10.35	0.010
2	22.52	0.065	22.52	0.032
3	37.33	0.133	37.33	0.066
4	54.35	0.224	54.35	0.112
5	73.32	0.339	73.32	0.170
6	94.06	0.478	94.06	0.239

Table 4.1: Real and imaginary frequencies for the first six axisymmetric modes from both irrotational and rotational analysis. Computations are for water at room temperature.

axisymmetric modes, $m = 0$. Recall that the rotational model was simplified by assuming axial symmetry, which is why only axisymmetric results are shown. In Table 4.1, λ_r is the rotational eigenvalue and λ_i is the irrotational eigenvalue. The results show that the real frequencies are the same for both the irrotational and rotational analysis; however, the imaginary frequencies differ, which correspond to the damping in the system. This is expected because the viscous term has a higher coefficient in the rotational analysis. In the irrotational analysis, the coefficient is 2, but in the rotational analysis presented here it is 4. The result is that the imaginary frequencies are twice the irrotational imaginary frequencies, which directly corresponds to the higher coefficient in the viscous term. Thus, including rotational effects does not alter the natural frequencies of the system, but simply increases the damping by a factor of two. Recall that this is only true with the assumption of small viscosity.

This results makes sense because damping, or viscous dissipation, is associated with movement in a system. In Table 4.1 we see that as n increases, both the real and imaginary frequencies increase, indicating that the damping increases as the real frequency of the mode increases. A higher frequency, which means greater motion in the system, leads to more damping in the system. In the irrotational analysis, however, we ignored all rotational fluid movement. Including the rotational movement should naturally lead to an increase of damping in the system. In this analysis it was shown that for small viscosity, an increase in damping is the only effect of the rotational fluid motion, and it was shown that the damping increases by a factor of two.

4.2.1 Varying Oh

The effect of allowing rotation for various Oh values is shown in Figure 4.2. The real natural frequency as Oh varies is shown in Figure 4.2a, while the imaginary frequency component is shown

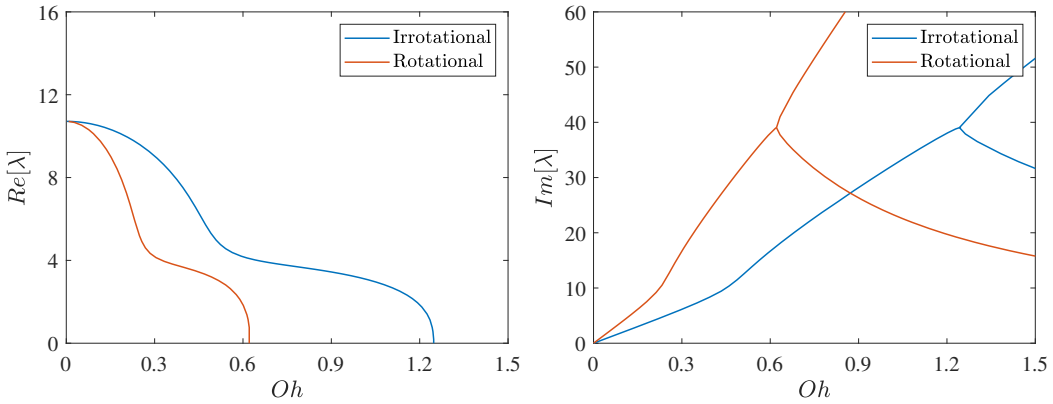

(a) Real frequency response

(b) Imaginary frequency response

Figure 4.2: Comparison of the irrotational and rotational frequency response as the Ohnesorge number is varied for the first axisymmetric mode ($n = 1$).

in Figure 4.2b. The change in frequency is shown for the $(1, 0)$ mode for both the irrotational and rotational analysis. Figure 4.2b shows that as Oh increases, the imaginary frequency, which corresponds to damping, increases twice as quickly when rotational effects are included. The result is that the rotational system becomes overdamped at a much lower Oh value. The critical damping point is signified by the pitchfork bifurcation of the imaginary frequency. The irrotational system becomes overdamped at $Oh = 1.25$, while the rotational system becomes overdamped at $Oh = 0.62$. In Figure 4.2a, the critical damping point is when the frequency decreases to zero. The increased damping means that the real rotational frequency decreases twice as quickly when Oh increases.

4.2.2 Forced comparison

The rotational effect is further illustrated by considering the response diagram of if the motion of the cylinder is forced. Using the same method as the irrotational analysis, a forced frequency response diagram was computed for the rotational model. The vertical axis represents the norm of the coefficient vector, which gives and indication of the magnitude of the surface perturbation. The peaks correspond to natural frequencies (mode frequencies). Figure 4.3 is for the axisymmetric case, where $m = 0$. The first peak corresponds to $n = 1$, the second to $n = 2$, and so on. The increased damping in the rotational case has no effect on the peak frequencies, which is consistent with the results in Table 4.1. However, the increased damping causes the peak amplitudes to decrease significantly, which is what we should expect.

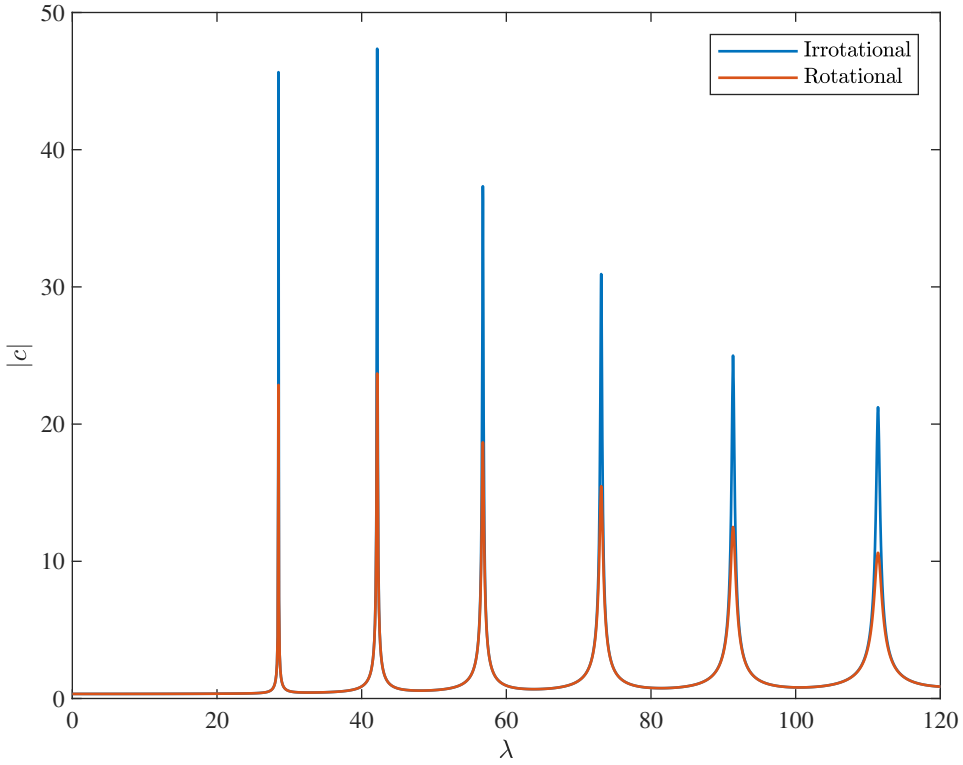

Figure 4.3: Comparison of the irrotational and rotational forced amplitude response as the nondimensional frequency λ is increased.

Chapter 5

Conclusion

A theoretical model for surfaces waves formed on a liquid contained in a cylindrical container with brimful conditions has been presented here. This model includes effects from viscosity, elasticity, surface tension, and gravity on the inertial movement of the fluid. The pinned edge boundary condition is included in the model by deriving modified basis functions in a constrained function space, which results an integro-differential equation governing the dynamics of the system. This governing equation is expressed as a nonlinear eigenvalue problem by transforming it into a matrix operator equation, with inertial, viscous, and restorative force operators. An approximate solution to this equation is achieved using a Rayleigh-Ritz variational procedure. This procedure allows for the shape and resonance frequency of any mode to be computed, given a set of physical parameters.

The effects of various parameters on the mode frequencies are explored. It is demonstrated that as the aspect ratio increases, the mode frequencies increase as well until plateauing at the infinite depth limit. While this limit is not constant (it decreases for higher modes), it is shown that this transition occurs at $h \sim 1$. It is demonstrated that the transition from capillary waves to capillary-gravity waves occurs at $Bo \sim 10$, and that the transition point increases as the mode increases. The transition from capillary waves to elastocapillary waves is shown to occur at $Ec \sim 1$. As with capillary-gravity waves, the transition point increases as the mode increases.

The Ohnesorge number is varied to study the its effects on the mode frequency. Unlike the other parameters, the Ohnesorge number effects both the real and imaginary parts of the mode frequency, the real component representing the actual resonance frequency and the imaginary component representing the viscous damping. The transition point from underdamped to overdamped

is observed when the real frequency decreases to zero. It is shown that this point decreases as the mode increases. This transition is the result of a pitchfork bifurcation in the imaginary component of the mode frequency. Curves are produced showing the critical damping transition point as a function of both the elastocapillary number and the Ohnesorge number. It is shown that increases in both Oh and Ec result in a higher critically damping point for the system.

A forced version of the governing integro-differential equation is derived and reduced to a simple linear matrix equation. The Rayleigh-Ritz method is again used to approximate a solution. Frequency sweeps are produced showing the amplitude response of the system across a range of driving frequency values. Peaks are identified which correspond precisely to the mode frequencies computed from the free model. A decrease in peak amplitude and spreading of the peak base as modes increase are observed, indicative of increased dissipation at higher modes. It is demonstrated that increasing the Ohnesorge number decreases the peak amplitudes with no impact on the peak frequencies. In contrast, increasing the elastocapillary number is shown to both increase the peak frequencies and decrease the peak amplitude. Higher modes are shown to exhibit a larger frequency shift.

The theoretical model is verified through comparison with experimental data obtained by Dr. Xingchen Shao. The overall agreement between the theory and experiment is excellent. The resonance frequencies for the first fifty modes are computed for water and almost all are within 1% of the experimental values. For glycerol/water mixtures with different Ohnesorge numbers, the theoretical frequencies computed have an average difference of 8% from the experimental values. Theoretical frequencies for agarose gels with various elastocapillary numbers have an average difference of 3.7%. Frequencies computed for two different aspect ratios ($h = 0.629$ and $h = 0.2$) have an average difference of 1.1% and 1.2%, respectively. Comparison is made for several modes with both pinned and sliding boundary conditions, with average difference of 1.4% and 1.6%, respectively.

A rotational model is also derived for the same system, using similar (although substantially different) methodology. This model is derived to examine the irrotational assumpion, and explore the effects of including fluid rotation. A governing integro-differential equation was derived governing the dynamics of the rotational system. Using a small viscosity assumption ($\mu << 1$), the governing equation is transformed into an operator equation of similar form to the irrotational model. It is demonstrated that, given $\mu << 1$, the only difference in the two models comes through the viscous operator, which is increased by a factor of two. Thus, it is demonstrated that rotational effects only

impact the dissipation in the system, while the mode frequencies remain unaffected. Practically, this means that the real mode frequencies are unchanged, but the imaginary component of the mode frequencies are doubled.

Further development of this theoretical work could include consideration of materials with complex (frequency dependent) rheology. In the theoretical analysis presented here, it is assumed that material properties are constant, since in the corresponding experimental studies materials were chosen that exhibit constant rheological properties over the range of frequencies investigated. However, many viscoelastic materials exhibit complex rheology, where the material behavior changes at a crossover frequency. Material behavior may transition from fluid-like (viscous) to solid-like (elastic) or vice versa, as in the case of shear-thickening (viscous to elastic) and shear-thinning (elastic to viscous) materials. The model derived in this thesis could be extended to investigate the complex dynamics of surface waves on these materials.

Appendices

Appendix A Derivation of the free surface curvature

The curvature of the free surface of the fluid is defined as the divergence of the surface normal. The following derivation demonstrates how a mathematical expression for the curvature in this problem is obtained. Naturally, this expression is derived in cylindrical coordinates. First, as in the problem presented in Chapter 2, the free surface is defined as

$$z = L + \varepsilon\eta, \tag{1}$$

with the $O(\varepsilon)$ surface perturbation defined as a function of r, θ, and t:

$$\eta(r, \theta, t) = y(r)e^{im\theta}e^{i\omega t} \tag{2}$$

Rearranging (1) gives

$$z - L - \varepsilon\eta = 0, \tag{3}$$

a function that is equal to zero at every point on the free surface. The surface normal vector can then be written as the gradient of this zero function:

$$\vec{n} = \nabla(z - L - \varepsilon\eta) \tag{4}$$

Likewise, the unit normal vector is obtained simply by dividing by the vector magnitude:

$$\hat{n} = \frac{\nabla(z - L - \varepsilon\eta)}{|\nabla(z - L - \varepsilon\eta)|} \tag{5}$$

Evaluating the numerator gives

$$\nabla(z - L - \varepsilon\eta) = \varepsilon\frac{\partial\eta}{\partial r}\hat{e}_r + \varepsilon\frac{1}{r}\frac{\partial\eta}{\partial\theta}\hat{e}_\theta + (1)\hat{e}_z. \tag{6}$$

Note that the first two terms are $O(\varepsilon)$ and the last term is $O(1)$. Evaluating the denominator gives

$$|\nabla(z - L - \varepsilon\eta)| = \sqrt{\left(\varepsilon\frac{\partial\eta}{\partial r}\right)^2 + \left(\varepsilon\frac{1}{r}\frac{\partial\eta}{\partial\theta}\right)^2 + (1)^2} \sim 1. \tag{7}$$

The first two terms under the radical are $O(\varepsilon^2)$ and hence very small, so the magnitude is approximately equal to 1. Thus, evaluating the partial derivatives in (6), the unit normal vector can be expressed as

$$\hat{n} = \varepsilon \frac{dy}{dr} e^{im\theta} e^{i\omega t} \hat{e}_r + \varepsilon \frac{1}{r} imy e^{im\theta} e^{i\omega t} \hat{e}_\theta + (1)\hat{e}_z. \tag{8}$$

Taking the divergence of the normal gives

$$\nabla \cdot \hat{n} = \frac{1}{r} \frac{\partial (r\varepsilon \frac{dy}{dr} e^{im\theta} e^{i\omega t})}{\partial r} + \frac{1}{r} \frac{\partial (\varepsilon \frac{1}{r} imy e^{im\theta} e^{i\omega t})}{\partial \theta} + \frac{\partial (1)}{\partial z}. \tag{9}$$

Evaluating the partial derivatives results in

$$\nabla \cdot \hat{n} = \varepsilon \frac{1}{r} \left[r \frac{d^2 y}{dr^2} + (1) \frac{dy}{dr} \right] e^{im\theta} e^{i\omega t} + \varepsilon \frac{1}{r^2} (-m^2) y e^{im\theta} e^{i\omega t}, \tag{10}$$

which can be simplified to

$$\nabla \cdot \hat{n} = \varepsilon \left[\frac{d^2 y}{dr^2} + \frac{1}{r} \frac{dy}{dr} - \frac{m^2}{r^2} y \right] e^{im\theta} e^{i\omega t}. \tag{11}$$

So, the $O(\varepsilon)$ divergence of the surface normal can be expressed as

$$\nabla \cdot \hat{n} = \left[\frac{d^2}{dr^2} + \frac{1}{r} \frac{d}{dr} - \frac{m^2}{r^2} \right] \eta. \tag{12}$$

Note that the time and azimuthal components of the surface perturbation η factor through in the problem solution method presented in Chapter 2. In this case, the divergence of the surface normal can be simplified and written in terms of y only:

$$\nabla \cdot \hat{n} = \left[\frac{d^2}{dr^2} + \frac{1}{r} \frac{d}{dr} - \frac{m^2}{r^2} \right] y. \tag{13}$$

Appendix B MATLAB Code for Rayleigh-Ritz Solution Method

B.1 Bessel Basis Functions

```
%% Bessel Basis Functions for Rayleigh-Ritz Solution Method
% Phillip Wilson

% Start timer
tic

% Opening commands
clear
clc
close all

% Input variables
m = 0; % Basis function order
N = 30; % Number of basis functions

%% Define roots
% This finds the non-zero roots of J' (the Bessel function derivative),
% which are the k values that are used to define the basis functions.

% Define zeros
Jm = chebfun(@(x) besselj(m,x),[0 1000]); % Define bessel function
Jmp = diff(Jm); % Differentiate function
k = roots(Jmp); % Determine the roots of the derivative

% Ensure that all the roots are non-zero
if k(1) == 0
    k(1) = [];
end

%% Define basis functions
% This defines an orthogonal set of basis functions in terms of the Bessel
% functions, which naturally satisfy the no penetration condition and a
% sliding contact line condition.

% Define basis functions in terms of the Bessel functions
```

```
x = chebfun('x',[0 1]);
J = cell(N,1);
for i = 1:N
    J{i} = besselj(m,k(i)*x);
end

%% Store basis functions
file = "W_Free_Basis_Functions_m_N30.mat";
filename = insertAfter(file,24,num2str(m));
save(filename)

% End timer
toc

% End code
```

B.2 Modiefied (Pinned) Basis Functions

```
%% Modified (Pinned) Basis Functions for Rayleigh-Ritz Solution Method
% Phillip Wilson

% Start timer
tic

% Opening commands
clear
clc
close all

% Input variables
m = 0; % Basis function order
N = 30; % Number of basis functions

%% Define roots
% This finds the non-zero roots of J' (the Bessel function derivative),
% which are the k values that are used to define the basis functions.

% Define roots of the Bessel function derivative
Jm = chebfun(@(x) besselj(m,x),[0 1000]); % Define bessel function
Jmp = diff(Jm); % Differentiate function
k = roots(Jmp); % Determine the roots of the derivative

% Ensure that all the roots are non-zero
if k(1) == 0
    k(1) = [];
end

%% Define basis functions
% This defines an orthogonal set of basis functions that satisfies the
% pinned boundary condition.

% Define set of non-orthogonal functions
x = chebfun('x',[0 1]);
P = cell(N+2,1);
for p = 1:N+2
```

```
38      P{p} = besselj(m,k(p)*x) - (besselj(m,k(p)*1)/besselj(m,k(1)*1))*besselj(m,k(1)*x
        );
39  end
40
41  % Othogonolize using the Grahm-Schmidt process
42  V = cell(N,1);
43  S = chebfun('0',[0 1]);
44  for i = 1:N
45      w = i;
46      V{i} = P{i+1} - S;
47
48      S = chebfun('0',[0 1]);
49      for j = 1:w
50          S = S + (sum(x*P{i+2}*V{j})/sum(x*V{j}*V{j}))*V{j};
51      end
52  end
53
54  %% Store basis functions
55  file = "W_Basis_Functions_m_N30.mat";
56  filename = insertAfter(file,19,num2str(m));
57  save(filename)
58
59  % End timer
60  toc
61
62  % End code
```

B.3 Expansion Matrices

```
%% Expansion Matrices for Rayleigh-Ritz Solution Method
% Phillip Wilson

% Begin timer
tic

% Opening commands
clear
clc
close all

% Input variables
m = 0; % Basis function order
N = 30; % Number of basis functions
h = 0.6286; % Aspect ratio

%% Load basis functions V{i}
% This loads the modified basis functions (which fulfilled the pinned edge
% condition) and the Bessel functions of the first kind.

% Load modified (pinned) basis functions
file = 'W_Basis_Functions_m_N30.mat';
filename = insertAfter(file,19,num2str(m));
load(filename,'V','k','x');

% Load ordinary Bessel functions
file = 'W_Free_Basis_Functions_m_N30.mat';
filename = insertAfter(file,24,num2str(m));
load(filename,'J');

%% Construct matrices
% This expands the governing operator equation into a matrix equation by
% taking inner products with the modified basis functions.

% Initialize the matrices
A0_1 = zeros(N); % Zeroth order matrix 1 (elasticity)
A0_2 = zeros(N); % Zeroth order matrix 2 (gravity)
```

```
A0_3 = zeros(N); % Zeroth order matrix 3 (surface tension)
A1 = zeros(N); % First order matrix (viscosity)
A2 = zeros(N); % Second order matrix (pressure)

% Compute matrices
for i = 1:1:N
    for j = 1:1:N
        % Zeroth order terms
        M0_1 = chebfun('0',[0 1]); % Initialize
        for n = 1:N % Apply operator (series)
            M0_1 = M0_1 + (k(n))*(1/tanh(k(n)*h))*(sum(x*V{i}*J{n})/sum(x*J{n}*J{n}))
    *J{n};
        end
        M0_1 = -M0_1; % Make negative
        A0_1(i,j) = sum(x*M0_1*V{j}); % Inner product

        M0_2 = -V{i}; % Apply operator
        A0_2(i,j) = sum(x*M0_2*V{j}); % Inner product

        M0_3 = diff(diff(V{i})) + (1/x)*diff(V{i}) - ((m^2)/(x^2))*V{i}; % Apply
    operator
        integrand = chebfun(x*M0_3*V{j},[0,1],'splitting','on'); % Split function
        A0_3(i,j) = sum(integrand); % Inner product

        % First order term
        M1 = chebfun('0',[0 1]); % Initialize
        for n = 1:N % Apply operator (series)
            M1 = M1 + (k(n))*(1/tanh(k(n)*h))*(sum(x*V{i}*J{n})/sum(x*J{n}*J{n}))*J{n
    };
        end
        M1 = -1i*M1; % Make negative and imaginary
        A1(i,j) = sum(x*M1*V{j}); % Inner product

        % Second order term
        M2 = chebfun('0',[0 1]); % Initialize
        for n = 1:N % Apply operator (series)
            M2 = M2 + (1/k(n))*(1/tanh(k(n)*h))*(sum(x*V{i}*J{n})/sum(x*J{n}*J{n}))*J
    {n};
        end
```

```
        A2(i,j) = sum(x*M2*V{j}); % Inner product
    end
end

%% Store expansion matrices
file = "W_Expansion_Matrices_m_N_hexp3.mat";
file = insertAfter(file,22,num2str(m));
filename = insertAfter(file,25,num2str(N));
save(filename)

% End timer
toc

% End code
```

B.4 Free Solution

```
%% Free Rayleigh-Ritz Solution for Cylinder Problem
% Phillip Wilson

% Begin timer
tic

% Opening commands
clear
clc
close all

%% Input variables
% Here all the relavent problem parameters are defined. This can be done in
% dimensional form, or via the dimensionless parameters.

% Initial parameters
m = 0; % Order
N = 30; % Length of series expansion

% Input parameters
r = 0.035; %0.0277; % Cylinder radius [m]
d = 0.022; %0.0380; % Cylinder depth [m]
y = 71.7*10^-3; % Surface tension [N/m]
u = 0.96*10^-3; % Viscosity [Pa-s]
s = 0; % Shear modulus [Pa]
g = 9.81; % Gravitational acceleration [m/s^2]
rho = 1000; % Density [kg/m^3]

% Define dimensionless parameters
h = d/r; % Aspect ratio
H = 'inf'; % Aspect ratio: equals 'exp' or 'inf'
Bo = (rho*g*r^2)/y; % Bond number
Oh2 = 2*(u/sqrt(rho*y*r)); % Ohnesorge number (times 2)
Ec2 = 2*((s*r)/y); % Elastocapillary number (times 2)

% Alternatively, directly input dimensionless parameters
% h = 1000; % Aspect ratio
```

```
% H = 'inf'; % Aspect ratio: equals 'exp' or 'inf'
% Bo = 150; % Bo number
% Oh2 = 1*2; % Ohnesorge number (times 2)
% Ec2 = 10*2; % Elastocapillary number (times 2)

%% Compute expansion matrices
% Here the generic expansion matrices are loaded, and the specific
% expansion matrices are computed using the dimensionless parameters.

% Load expansion matrices A0,A1,A2
file2 = 'W_Expansion_Matrices_m_N_h3.mat';
file2 = insertAfter(file2,22,num2str(m));
file2 = insertAfter(file2,25,num2str(N));
filename2 = insertAfter(file2,29,num2str(H));
load(filename2,'A0_1','A0_2','A0_3','A1','A2');

% Compute specific matrices
spec_A0 = Ec2*A0_1 + Bo*A0_2 + A0_3;
spec_A1 = Oh2*A1;
spec_A2 = A2;

%% Solve for eigenvalues
% This solves the polynomical eigenvalue problem and sorts the resulting
% eigenvalues and eigenvectors.

% Extract eigenvalues and eigenvectors
[Vec,Eig] = polyeig(spec_A0,spec_A1,spec_A2);

% Sort eigenvalues
[Eval_Sorted,Index] = sort(Eig,'ComparisonMethod','real');
Eval_Filtered = zeros(N,1);
for i = 1:N
    Eval_Filtered(i) = Eval_Sorted(N+i);
end

% Sort eigenvectors
Evec_Filtered = zeros(N,N);
for j = 1:N
Evec_Filtered(:,j) = Vec(:,Index(N+j));
```

```
end

% Separate eigenvalues into real and imaginary components
reig = real(Eval_Filtered); % Real eigenvalues
ieig = imag(Eval_Filtered); % Imaginary eigenvalues
c = real(Evec_Filtered); % Real eigenvectors

% Convert eigenvalues to dimensional frequencies
lamda = (Eval_Filtered.^2)/Bo;
f = sqrt(lamda*9.81/r)/(2*pi);
fr = real(f); % Real dimensional frequencies

% End timer
toc

% End code
```

B.5 Forced Solution

```
%% Forced Rayleigh-Ritz Solution for Cylinder Problem
% Phillip Wilson

% Begin timer
tic

% Opening commands
clear
clc
close all

%% Input variables
% Here all the relavent problem parameters are defined.

% Initial parameters
m = 0; % Order
N = 30; % Length of series expansion

% Response diagram parameters
Freq_min = 0; % Minimum frequency value (in Hz)
Freq_max = 25; % Maximum frequency value (in Hz)
grid = 50000; % Number of grid points

% System parameters
r = 0.035; % Cylinder radius [m]
d = 0.022; % Cylinder depth [m]
y = 71.7*10^-3; % Surface tension [N/m]
u = 0.96*10^-3; % Viscosity(index)*10^-3; % Viscosity [Pa-s]
s = 20.2; % Shear modulus [Pa]
g = 9.81; % Gravitational acceleration [m/s^2]
rho = 1000; % Density [kg/m^3]

% Dimensionless parameters
h = d/r; % Aspect ratio
H = 'exp'; % Aspect ratio: equals 'exp' or 'inf'
Bo = (rho*g*r^2)/y; % Bond number
Oh2 = 2*(u/sqrt(rho*y*r)); % Ohnesorge number (times 2)
```

```
Ec2 = 2*((s*r)/y); % Elastocapillary number (times 2)

%% Load expansion matrices
% This loads the generic expansion matrices which are used to compute the
% frequency response.

% Load expansion matrices A0,A1,A2
file2 = 'W_Expansion_Matrices_m_N_h3.mat';
file2 = insertAfter(file2,22,num2str(m));
file2 = insertAfter(file2,25,num2str(N));
filename2 = insertAfter(file2,29,num2str(H));
load(filename2,'A0_1','A0_2','A0_3','A1','A2');

%% Compute frequency sweep
% This computes frequency response data over the range specified above by
% solving the linear matrix equation Ac=B for each frequency value.

% Define B matrix (representing uniform acceleration if the cylinder)
B = ones(30,1);

% Begin frequency variation loop
Freq_val = transpose(linspace(Freq_min,Freq_max,grid)); % Frequency values
C = zeros(grid,1); % Initialize amplitude vector
q = 0;
for l = Freq_min:(Freq_max-Freq_min)/(grid-1):Freq_max
    q = q + 1;

    e = sqrt((rho*((2*pi*l)^2)*(r^3))/y); % Dimensionless driving frequency

    A = Ec2*A0_1 + Bo*A0_2 + A0_3 + e*Oh2*A1 +(e^2)*A2;

    c = linsolve(A,B); % Solve the linear matrix equation
    C(q,1) = norm(c); % Represent amplitude as norm of coefficient vector
end

%% Plot frequency response diagram
% This plots the norm of the coefficient vector c (which corresponds to
% amplitude) against the driving frequency in Hz.

```

```
77 % Plot
78 figure % Create figure
79 plot(Freq_val,C) % Plot the frequency response diagram
80
81 % Axis labels
82 xlabel('f [Hz]')
83 ylabel('|c|')
84
85 % End timer
86 toc
87
88 % End code
```

Appendix C MATLAB Code for Parameter Analysis

C.1 h Paramater Variation Analysis

```
%% h Parameter Variation Analysis
% Phillip Wilson

% Begin timer
tic

% Opening commands
clear
clc
close all

%% Input variables
% Here all the relavent problem parameters are defined. This can be done in
% dimensional form, or via the dimensionless parameters.

% Initial parameters
m = 0; % Order
N = 30; % Length of series expansion

% Input parameters
r = 0.035; %0.0277; % Cylinder radius [m]
d = 0.022; %0.0380; % Cylinder depth [m]
y = 71.7*10^-3; % Surface tension [N/m]
u = 0.96*10^-3; % Viscosity [Pa-s]
s = 0; % Shear modulus [Pa]
g = 9.81; % Gravitational acceleration [m/s^2]
rho = 1000; % Density [kg/m^3]

% Define dimensionless parameters
h = d/r; % Aspect ratio
H = 'inf'; % Aspect ratio: equals 'exp' or 'inf'
Bo = (rho*g*r^2)/y; % Bond number
Oh2 = 2*(u/sqrt(rho*y*r)); % Ohnesorge number (times 2)
Ec2 = 2*((s*r)/y); % Elastocapillary number (times 2)

```

```
% Alternatively, directly input dimensionless parameters
% h = 1000; % Aspect ratio
% H = 'inf'; % Aspect ratio: equals 'exp' or 'inf'
% Bo = 150; % Bo number
% Oh2 = 1*2; % Ohnesorge number (times 2)
% Ec2 = 10*2; % Elastocapillary number (times 2)

%% Load basis functions
% This loads the modified basis functions (which fulfilled the pinned edge
% condition) and the Bessel functions of the first kind.

% Load modified (pinned) basis functions
file = 'W_Basis_Functions_m_N30.mat';
filename = insertAfter(file,19,num2str(m));
load(filename,'V','k','x');

% Load ordinary Bessel functions
file = 'W_Free_Basis_Functions_m_N30.mat';
filename = insertAfter(file,24,num2str(m));
load(filename,'J');

%% Load expansion matrices
% Here the first and second parts of the generic zeroth order expansion
% matricix are loaded. All other matrices are a function of h and must be
% recalculated for each h value.

% Load expansion matrices A0_2,A0_3
file2 = 'W_Expansion_Matrices_m_N_h3.mat';
file2 = insertAfter(file2,22,num2str(m));
file2 = insertAfter(file2,25,num2str(N));
filename2 = insertAfter(file2,29,num2str(H));
load(filename2,'A0_2','A0_3');

%% Calculate results for h variation
% This calculates the frequency over a range of h values. Note that the
% h values are defined logarithmically, as the results are best displayed
% on a semilog plot.

% Define logarithmic h values
```

```
grid = 3; % Number of grid points
ii = linspace(-3,2,grid);
h_val = zeros(grid,1);
for kk = 1:1:grid
    h_val(kk,1) = 10^ii(kk);
end

% Initialize counter
t = 0;

% Initialize frequency vectors
Realn1 = zeros(grid,1);
Realn2 = zeros(grid,1);
Realn3 = zeros(grid,1);

% Calculate frequency values
for hi = 1:1:grid
h = h_val(hi);

t = t +1;

% Initialize expansion matrices
A0_1 = zeros(N); % First zeroth order matrix
A1 = zeros(N); % First order matrix
A2 = zeros(N); % Second order matrix

% Compute expansion matrices
for i = 1:1:N
    for j = 1:1:N
        % Zeroth order terms
        M0_1 = chebfun('0',[0 1]); % Initialize
        for n = 1:N % Apply operator (series)
            M0_1 = M0_1 + (k(n))*(1/tanh(k(n)*h))*(sum(x*V{i}*J{n})/sum(x*J{n}*J{n}))
    *J{n};
        end
        M0_1 = -M0_1; % Make negative
        A0_1(i,j) = sum(x*M0_1*V{j}); % Inner product

        % First order term
```

```
        M1 = chebfun('0',[0 1]); % Initialize
        for n = 1:N % Apply operator (series)
            M1 = M1 + (k(n))*(1/tanh(k(n)*h))*(sum(x*V{i}*J{n})/sum(x*J{n}*J{n}))*J{n
    };
        end
        M1 = -1i*M1; % Make negative and imaginary
        A1(i,j) = sum(x*M1*V{j}); % Inner product

        % Second order term
        M2 = chebfun('0',[0 1]); % Initialize
        for n = 1:N % Apply operator (series)
            M2 = M2 + (1/k(n))*(1/tanh(k(n)*h))*(sum(x*V{i}*J{n})/sum(x*J{n}*J{n}))*J
    {n};
        end
        A2(i,j) = sum(x*M2*V{j}); % Inner product
    end
end

% Define specific expansion matrices
A0 = Ec2*A0_1 + Bo*A0_2 + A0_3;
A1 = Oh2*A1;

% Extract eigenvalues and eigenvectors
[Vec,Eig] = polyeig(A0,A1,A2);

% Sort eigenvalues
[Eval_Sorted,Index] = sort(Eig,'ComparisonMethod','real');
Eval_Filtered = zeros(N,1);
for i = 1:N
    Eval_Filtered(i) = Eval_Sorted(N+i);
end

% Sort eigenvectors
Evec_Filtered = zeros(N,N);
for i = 1:N
Evec_Filtered(:,i) = Vec(:,Index(N+i));
end

Realn1(t,1) = real(Eval_Filtered(1));
```

```
Realn2(t,1) = real(Eval_Filtered(2));
Realn3(t,1) = real(Eval_Filtered(3));

disp(t)
end

%% Make plot
% This creates a semilog plot of the first three modes.

% Plot
figure
semilogx(h_val,Realn1,'-b',h_val,Realn2,'--b',h_val,Realn3,':b','LineWidth',1.5)

% Set axis properties
xlim([10^-3 10^2])
set(gca,'Units','normalized','Position',[0.1 0.1 0.8 0.8],'FontSize',9,'FontName','
    Times')
xlabel('$h$','interpreter','latex','FontSize',10)
ylabel('$\lambda$','interpreter','latex','FontSize',10)
legend("(1," + m + ")","(2," + m + ")","(3," + m + ")",'interpreter','latex','
    FontSize',8,'Location','NorthWest')

% End timer
toc

% End code
```

C.2 Bo Paramater Variation Analysis

```
%% Bo Parameter Variation Analysis
% Phillip Wilson

% Begin timer
tic

% Opening commands
clear
clc
close all

%% Input variables
% Here all the relavent problem parameters are defined. This can be done in
% dimensional form, or via the dimensionless parameters.

% Initial parameters
m = 0; % Order
N = 30; % Length of series expansion

% Input parameters
r = 0.035; %0.0277; % Cylinder radius [m]
d = 0.022; %0.0380; % Cylinder depth [m]
y = 71.7*10^-3; % Surface tension [N/m]
u = 0.96*10^-3; % Viscosity [Pa-s]
s = 0; % Shear modulus [Pa]
g = 9.81; % Gravitational acceleration [m/s^2]
rho = 1000; % Density [kg/m^3]

% Define dimensionless parameters
h = d/r; % Aspect ratio
H = 'inf'; % Aspect ratio: equals 'exp' or 'inf'
Bo = (rho*g*r^2)/y; % Bond number
Oh2 = 2*(u/sqrt(rho*y*r)); % Ohnesorge number (times 2)
Ec2 = 2*((s*r)/y); % Elastocapillary number (times 2)

% Alternatively, directly input dimensionless parameters
% h = 1000; % Aspect ratio
```

```
% H = 'inf'; % Aspect ratio: equals 'exp' or 'inf'
% Bo = 150; % Bo number
% Oh2 = 1*2; % Ohnesorge number (times 2)
% Ec2 = 10*2; % Elastocapillary number (times 2)

%% Compute expansion matrices
% Here the generic expansion matrices are loaded, and the specific
% expansion matrices are computed using the dimensionless parameters.

% Load expansion matrices A0,A1,A2
file2 = 'W_Expansion_Matrices_m_N_h3.mat';
file2 = insertAfter(file2,22,num2str(m));
file2 = insertAfter(file2,25,num2str(N));
filename2 = insertAfter(file2,29,num2str(H));
load(filename2,'A0_1','A0_2','A0_3','A1','A2');

% Define fixed matrices
Bo_A1 = Oh2*A1;
Bo_A2 = A2;

%% Calculate results for Bo variation
% This calculates the frequency over a range of Bo numbers. Note that the
% Bo numbers are defined logarithmically, as the results are best displayed
% on a log-log plot.

% Define logarithmic Bo values
grid = 100; % Number of grid points
ii = linspace(-3,3,grid);
Bo_val = zeros(grid,1);
for kk = 1:1:grid
    Bo_val(kk,1) = 10^ii(kk);
end

% Initialize counter
j = 0;

% Initialize frequency vectors
Realn1 = zeros(grid,1);
Realn2 = zeros(grid,1);
```

```
Realn3 = zeros(grid,1);

% Calcullate frequency values
for bi = 1:1:grid
Bo = Bo_val(bi);

j = j + 1;

% Compute matrices
Bo_A0 = Ec2*A0_1 + Bo*A0_2 + A0_3;

% Extract eigenvalues and eigenvectors
[Vec,Eig] = polyeig(Bo_A0,Bo_A1,Bo_A2);

% Sort eigenvalues
[Eval_Sorted,Index] = sort(Eig,'ComparisonMethod','real');
Eval_Filtered = zeros(N,1);
for i = 1:N
    Eval_Filtered(i) = Eval_Sorted(N+i);
end

% Sort eigenvectors
Evec_Filtered = zeros(N,N);
for i = 1:N
Evec_Filtered(:,i) = Vec(:,Index(N+i));
end

% Store real eigenvalues for the first three modes
Realn1(j,1) = real(Eval_Filtered(1));
Realn2(j,1) = real(Eval_Filtered(2));
Realn3(j,1) = real(Eval_Filtered(3));

end

%% Make plot
% This creates a log-log plot of the first three modes.

% Plot
figure
```

```
116 loglog(Bo_val,Realn1,'-b',Bo_val,Realn2,'--b',Bo_val,Realn3,':b','LineWidth',1.5)
117
118 % Set axis properties
119 xlim([10^-3 10^3])
120 set(gca,'Units','normalized','Position',[0.1 0.1 0.8 0.8],'FontSize',9,'FontName','
        Times')
121 xlabel('$Bo$','interpreter','latex','FontSize',10)
122 ylabel('$\lambda$','interpreter','latex','FontSize',10)
123 legend("(1," + m + ")","(2," + m + ")","(3," + m + ")",'interpreter','latex','
        FontSize',8,'Location','NorthWest')
124
125 % End timer
126 toc
127
128 % End code
```

C.3 Ec Paramater Variation Analysis

```
%% Ec Parameter Variation Analysis
% Phillip Wilson

% Begin timer
tic

% Opening commands
clear
clc
close all

%% Input variables
% Here all the relavent problem parameters are defined. This can be done in
% dimensional form, or via the dimensionless parameters.

% Initial parameters
m = 0; % Order
N = 30; % Length of series expansion

% Input parameters
r = 0.035; %0.0277; % Cylinder radius [m]
d = 0.022; %0.0380; % Cylinder depth [m]
y = 71.7*10^-3; % Surface tension [N/m]
u = 0.96*10^-3; % Viscosity [Pa-s]
s = 0; % Shear modulus [Pa]
g = 9.81; % Gravitational acceleration [m/s^2]
rho = 1000; % Density [kg/m^3]

% Define dimensionless parameters
h = d/r; % Aspect ratio
H = 'inf'; % Aspect ratio: equals 'exp' or 'inf'
Bo = (rho*g*r^2)/y; % Bond number
Oh2 = 2*(u/sqrt(rho*y*r)); % Ohnesorge number (times 2)
Ec2 = 2*((s*r)/y); % Elastocapillary number (times 2)

% Alternatively, directly input dimensionless parameters
% h = 1000; % Aspect ratio
```

```
% H = 'inf'; % Aspect ratio: equals 'exp' or 'inf'
% Bo = 150; % Bo number
% Oh2 = 1*2; % Ohnesorge number (times 2)
% Ec2 = 10*2; % Elastocapillary number (times 2)

%% Compute expansion matrices
% Here the generic expansion matrices are loaded, and the specific
% expansion matrices are computed using the dimensionless parameters.

% Load expansion matrices A0,A1,A2
file2 = 'W_Expansion_Matrices_m_N_h3.mat';
file2 = insertAfter(file2,22,num2str(m));
file2 = insertAfter(file2,25,num2str(N));
filename2 = insertAfter(file2,29,num2str(H));
load(filename2,'A0_1','A0_2','A0_3','A1','A2');

% Define fixed matrices
Ec_A1 = Oh2*A1;
Ec_A2 = A2;

%% Calculate results for Ec variation
% This calculates the frequency over a range of Ec numbers. Note that the
% Bo numbers are defined logarithmically, as the results are best displayed
% on a log-log plot.

% Define logarithmic Ec values
grid = 100; % Number of grid points
ii = linspace(-3,3,grid);
Ec2_val = zeros(grid,1);
for kk = 1:1:grid
    Ec2_val(kk,1) = 10^ii(kk)*2;
end

% Initialize counter
j = 0;

% Initialize frequency vectors
Realn1 = zeros(grid,1);
Realn2 = zeros(grid,1);
```

```
Realn3 = zeros(grid,1);

% Calculate frequency values
for ei = 1:1:grid
    Ec2 = Ec2_val(ei);

j = j + 1;

% Compute matrices
Ec_A0 = Ec2*A0_1 + Bo*A0_2 + A0_3;

% Extract eigenvalues and eigenvectors
[Vec,Eig] = polyeig(Ec_A0,Ec_A1,Ec_A2);

% Sort eigenvalues
[Eval_Sorted,Index] = sort(Eig,'ComparisonMethod','real');
Eval_Filtered = zeros(N,1);
for i = 1:N
    Eval_Filtered(i) = Eval_Sorted(N+i);
end

% Sort eigenvectors
Evec_Filtered = zeros(N,N);
for i = 1:N
Evec_Filtered(:,i) = Vec(:,Index(N+i));
end

% Store real eigenvalues for the first three modes
Realn1(j,1) = real(Eval_Filtered(1));
Realn2(j,1) = real(Eval_Filtered(2));
Realn3(j,1) = real(Eval_Filtered(3));

end

% Adjust Ec value
Ec_val = Ec2_val/2;

%% Make plot
% This creates a log-log plot of the first three modes.
```

```
116
117 % Plot
118 figure
119 loglog(Ec_val,Realn1,'-b',Ec_val,Realn2,'--b',Ec_val,Realn3,':b','LineWidth',1.5)
120
121 % Set axis properties
122 xlim([10^-3 10^3])
123 set(gca,'Units','normalized','Position',[0.1 0.1 0.8 0.8],'FontSize',9,'FontName','
    Times')
124 xlabel('$E$','interpreter','latex','FontSize',10)
125 ylabel('$Re[\lambda]$','interpreter','latex','FontSize',10)
126 legend("(1," + m + ")","(2," + m + ")","(3," + m + ")",'interpreter','latex','
    FontSize',8,'Location','NorthWest')
127
128 % End timer
129 toc
130
131 % End code
```

C.4 Oh Paramater Variation Analysis

```
%% Oh Parameter Variation Analysis
% Phillip Wilson

% Begin timer
tic

% Opening commands
clear
clc
close all

%% Input variables
% Here all the relavent problem parameters are defined. This can be done in
% dimensional form, or via the dimensionless parameters.

% Initial parameters
m = 0; % Order
N = 30; % Length of series expansion

% Input parameters
r = 0.035; %0.0277; % Cylinder radius [m]
d = 0.022; %0.0380; % Cylinder depth [m]
y = 71.7*10^-3; % Surface tension [N/m]
u = 0.96*10^-3; % Viscosity [Pa-s]
s = 0; % Shear modulus [Pa]
g = 9.81; % Gravitational acceleration [m/s^2]
rho = 1000; % Density [kg/m^3]

% Define dimensionless parameters
h = d/r; % Aspect ratio
H = 'inf'; % Aspect ratio: equals 'exp' or 'inf'
Bo = (rho*g*r^2)/y; % Bond number
Oh2 = 2*(u/sqrt(rho*y*r)); % Ohnesorge number (times 2)
Ec2 = 2*((s*r)/y); % Elastocapillary number (times 2)

% Alternatively, directly input dimensionless parameters
% h = 1000; % Aspect ratio
```

```
% H = 'inf'; % Aspect ratio: equals 'exp' or 'inf'
% Bo = 150; % Bo number
% Oh2 = 1*2; % Ohnesorge number (times 2)
% Ec2 = 10*2; % Elastocapillary number (times 2)

%% Compute expansion matrices
% Here the generic expansion matrices are loaded, and the specific
% expansion matrices are computed using the dimensionless parameters.

% Load expansion matrices A0,A1,A2
file2 = 'W_Expansion_Matrices_m_N_h3.mat';
file2 = insertAfter(file2,22,num2str(m));
file2 = insertAfter(file2,25,num2str(N));
filename2 = insertAfter(file2,29,num2str(H));
load(filename2,'A0_1','A0_2','A0_3','A1','A2');

% Define fixed matrices
Oh_A0 = Ec2*A0_1 + Bo*A0_2 + A0_3;
Oh_A2 = A2;

%% Calculate and plot results for Oh variation
% This calculates the frequency over a range of Oh numbers. Because it is
% difficult to isolate individual modes, all of the modes are plotted.
% Either the real or imaginary frequencies are plotted.

% Define parameter range and grid
Oh_min = 0; % Minimum value
Oh_max = 5; % Maximum value
grid = 500; % Number of points

% Define Oh values
Oh_val = linspace(Oh_min,Oh_max,grid);

% Initialize counter
j = 0;

% Calculate and plot frequency values
figure
for Oh = Oh_min:(Oh_max-Oh_min)/(grid-1):Oh_max
```

```
77
78 j = j+1;
79
80 % Compute matrices
81 Oh_A1 = 2*Oh*A1;
82
83 % Extract eigenvalues
84 [Vec,Eig] = polyeig(Oh_A0,Oh_A1,Oh_A2);
85
86 % Select either real or imaginary eigenvalues
87 Eval_Filtered = real(Eig( Eig>0 )); % Use real() or imag()
88
89 % Plot eigenvalues
90 hold on
91 plot(Oh,Eval_Filtered,'.')
92
93 end
94
95 % Set axis properties
96 ylim([0 100])
97 set(gca,'Units','normalized','Position',[0.1 0.1 0.8 0.8],'FontSize',9,'FontName','
       Times')
98 xlabel('$Oh$','interpreter','latex','FontSize',10)
99 ylabel('$Re[\lambda]$','interpreter','latex','FontSize',10)
100
101 % End timer
102 toc
103
104 % End code
```

Appendix D MATLAB Code for Mode Visualization

D.1 3D Shape Visualization

```
%% 3D Shape Visualization of Cylindrical Modes
% Phillip Wilson

% Start timer
tic

% Opening commands
clear
clc
% close all

% Input variables
n = 1; % Radial wavenumber
m = 0; % Azimuthal wavenumber (order)
N = 30; % Number of basis functions

%% Load basis functions and coefficients
% This loads both the modified (pinned) basis functions and the coefficient
% vector for the specified mode.

% Load basis functions V{i}
file = 'W_Basis_Functions_m_N30.mat';
filename = insertAfter(file,19,num2str(m));
load(filename,'V')

% Load coefficients c
file = 'W_Natural_m_V1.01_N30_hinf.mat';
filename = insertAfter(file,11,num2str(m));
load(filename,'c')
c = c(:,n);

%% Define surface
% This uses the coefficient vector c and the basis functions V to compute
% a function z defining the perturbed free surface.

```

```
% Define shape function
z = chebfun('0',[0 1]);
for i = 1:N
    z = z + c(i)*V{i};
end

%% Make 3D plot
% This plots the surface shape as well as a visual of the cylinder
% containing the fluid.

% Create 3D mesh
Grid = 100; % Grid size
r = linspace(0,1,Grid); % Define radial points
th = linspace(0,2*pi,Grid); % Define azimuthal points
[R,TH] = meshgrid(r,th); % Create a meshgrid
Z = 0.2*z(R).*cos(m.*TH); % Calculate meshgrid surface

% Plot cylinder
figure
[x,y,z] = cylinder(1.05,50); % Create cylinder
h1 = surf(x,y,z,'FaceColor', [0,0,0]); % Plot cylinder

% Plot surface
hold on
h2 = surfl(R.*cos(TH), R.*sin(TH), Z+1); % Plot surface z
colormap(gray) % Change color map to gray
set(h2, 'EdgeColor', 'interp', 'FaceColor', 'interp'); % Interpolate colors across
    lines and faces

% Adjust plot settings
axis vis3d % 3D axis view
grid off % Turn of grid
set(gca,'visible','off','xtick',[]) % Turn off axis scales
set(gca,'YTick',[],'XTick',-1:1:1,'Units','normalized','Position',[0 0 1 1],'FontSize
    ',9,'FontName','Times')

%% Print
print('3dshapem0n1_exp','-depsc') % Print as an eps file

```

```
73 % End timer
74 toc
75
76 % End code
```

D.2 2D Shape Visualization

```
%% 2D Shape Visualization of Cylindrical Modes
% Phillip Wilson

% Start timer
tic

% Opening commands
clear
clc
close all

% Input variables
n = 1; % Radial wavenumber
m = 0; % Azimuthal wavenumber (order)
N = 30; % Number of basis functions

%% Load basis functions and coefficients
% This loads both the modified (pinned) basis functions and the coefficient
% vector for the specified mode.

% Load basis functions V{i}
file = 'W_Basis_Functions_m_N30.mat';
filename = insertAfter(file,19,num2str(m));
load(filename,'V')

% Load coefficients c
file = 'W_Natural_m_V1.01_N30_hinf.mat';
filename = insertAfter(file,11,num2str(m));
load(filename,'c')
c = c(:,n);

%% Define surface
% This uses the coefficient vector c and the basis functions V to compute
% a function z defining the perturbed free surface.

% Define shape function
z = chebfun('0',[0 1]);
```

```
for i = 1:N
    z = z + c(i)*V{i};
end

%% Make 2D plot
% This plots the surface shape as well as a visual of the cylinder
% containing the fluid.

% Calculate surface values
e = 0.1;
grid = 100;
r1 = linspace(0,1,grid);
r2 = linspace(0,-1,grid);
zval = e*z(r1) + 0.6286;

% Plot surface
figure
plot(r1,zval,':k','LineWidth',1.5)
hold on
plot(r2,zval,':k','LineWidth',1.5)

% Plot cylinder
hold on
rectangle('Position',[-1 0 2 0.6286],'LineWidth',1.5)

% Set axis properties
axis([-1 1 0 0.8])
set(gca,'YTick',[],'XTick',[],'Units','normalized','Position',[0.2 0.1 0.6 0.8],'
    FontSize',9,'FontName','Times')

%% Print
print('shapem0n1','-depsc') % Print as an eps file

% End timer
toc

% End code
```

D.3 Pressure Visualization

```
%% Pressure Visualization of Cylindrical Modes
% Phillip Wilson

% Start timer
tic

% Opening commands
clear
clc
close all

% Input variables
n = 1; % Radial wavenumber
m = 0; % Azimuthal wavenumber (order)
N = 30; % Number of basis functions

%% Load basis functions and coefficients
% This loads both the modified (pinned) basis functions and the coefficient
% vector for the specified mode.

% Load basis functions V{i}
file = 'W_Basis_Functions_m_N30.mat';
filename = insertAfter(file,19,num2str(m));
load(filename,'V','k','x')

% Load coefficients c
file = 'W_Natural_m_V1.01_N30_hinf.mat';
filename = insertAfter(file,11,num2str(m));
load(filename,'c','h')
c = c(:,n);

%% Define surface
% This uses the coefficient vector c and the basis functions V to compute
% a function z defining the perturbed free surface.

% Define shape function
z = chebfun('0',[0 1]);
```

```
for i = 1:N
    z = z + c(i)*V{i};
end
Eta = z;

%% Calculate pressure
% This creates a meshgrid of a 2D cross section of the cylinder and then
% evaluates the pressure at each point.

% Create meshgrid
grid = 10;
r = linspace(0,1,grid);
z = linspace(0,0.6286,grid);
[R,Z] = meshgrid(r,z);
ETA = Eta(R);

% Evaluate pressure at each point
p = zeros(grid,grid);
for i = 1:grid
    for j = 1:grid
        for l = 1:N
            Jm = V{l};
            p(i,j) = p(i,j) + (1/k(l))*(cosh(k(l)*Z(i,j))/sinh(k(l)*h))*(sum(x*ETA(i,
    j)*V{l})/sum(x*V{l}*V{l}))*Jm(R(i,j));
        end
    end
end

%% Make plot
% This plots the pressure distribution as well as a visual of the cylinder
% containing the fluid.

% Plot pressure
figure
contourf(R,Z,p)
hold on
contourf(-R,Z,p)

% Plot cylinder
```

```
hold on
rectangle('Position',[-1 0 2 0.6286],'LineWidth',1.5)

% Set axis properties
axis([-1 1 0 0.8])
set(gca,'YTick',[],'XTick',[],'Units','normalized','Position',[0.2 0.1 0.6 0.8],'
    FontSize',9,'FontName','Times')

%% Print
print('pressurem0n1','-depsc') % Print as an eps file

% End timer
toc

% End code
```

D.4 Velocity Visualization

```
%% Velocity Visualization of Cylindrical Modes
% Phillip Wilson

% Start timer
tic

% Opening commands
clear
clc
close all

% Input variables
n = 1; % Radial wavenumber
m = 0; % Azimuthal wavenumber (order)
N = 30; % Number of basis functions

%% Load basis functions and coefficients
% This loads both the modified (pinned) basis functions and the coefficient
% vector for the specified mode.

% Load basis functions V{i}
file = 'W_Basis_Functions_m_N30.mat';
filename = insertAfter(file,19,num2str(m));
load(filename,'V','k','x')

% Load coefficients c
file = 'W_Natural_m_V1.01_N30_hinf.mat';
filename = insertAfter(file,11,num2str(m));
load(filename,'c','h')
c = c(:,n);

%% Define surface
% This uses the coefficient vector c and the basis functions V to compute
% a function z defining the perturbed free surface.

% Define shape function
z = chebfun('0',[0 1]);
```

```
for i = 1:N
    z = z + c(i)*V{i};
end
Eta = z;

%% Calculate velocity
% This creates a meshgrid of a 2D cross section of the cylinder and then
% evaluates the velocity vector at each point.

% Create meshgrid
grid = 10;
r = linspace(0.1,1,grid);
z = linspace(0,0.6286,grid);
[R,Z] = meshgrid(r,z);
ETA = Eta(R);

% Evaluate velocity potential at each point
ph = zeros(grid,grid);
for i = 1:grid
    for j = 1:grid
        for l = 1:N
            Jm = V{l};
            ph(i,j) = ph(i,j) + (1/k(l))*(cosh(k(l)*Z(i,j))/sinh(k(l)*h))*(sum(x*ETA(
    i,j)*V{l})/sum(x*V{l}*V{l}))*Jm(R(i,j));
        end
    end
end

% Calculate velocity vector components at each point
[U,V] = gradient(ph);
UN = U./sqrt(U.^2+V.^2);
VN = V./sqrt(U.^2+V.^2);

%% Make plot
% This plots the velocity field as well as a visual of the cylinder
% containing the fluid.

% Plot velocity
figure
```

```
quiver(R,Z,UN,VN,'AutoScale','on','AutoScaleFactor',0.3,'Color','k')
hold on
quiver(-R,Z,-UN,VN,'AutoScale','on','AutoScaleFactor',0.3,'Color','k')

% Plot cylinder
hold on
rectangle('Position',[-1 0 2 0.6286],'LineWidth',1.5)

% Set axis properties
axis([-1 1 0 0.8])
set(gca,'YTick',[],'XTick',[],'Units','normalized','Position',[0.2 0.1 0.6 0.8],'
    FontSize',9,'FontName','Times')

%% Print
print('velocitym0n1','-depsc') % Print as an eps file

% End timer
toc

% End code
```

D.5 Slope Magnitude Visualization

```
%% Slope Magnitude Visualization of Cylindrical Modes
% Phillip Wilson

% Start timer
tic

% Opening commands
clear
clc
close all

% Input variables
n = 1; % Radial wavenumber
m = 0; % Azimuthal wavenumber (order)
N = 30; % Number of basis functions

%% Load basis functions and coefficients
% This loads both the modified (pinned) basis functions and the coefficient
% vector for the specified mode.

% Load basis functions V{i}
file = 'W_Basis_Functions_m_N30.mat';
filename = insertAfter(file,19,num2str(m));
load(filename,'V')

% Load coefficients c
file = 'W_Natural_m_V1.01_N30_hexp.mat';
filename = insertAfter(file,11,num2str(m));
load(filename,'c')
c = c(:,n);

%% Define surface
% This uses the coefficient vector c and the basis functions V to compute
% a function z defining the perturbed free surface.

% Define shape function
z = chebfun('0',[0 1]);
```

```
for i = 1:N
    z = z + c(i)*V{i};
end

%% Calculate slope magnitude
% This creates a meshgrid of the cylinder surface and then calculates the
% wave slope magnitude at each point.

% Create meshgrid
Grid = 100;
r = linspace(0,1,Grid);
th = linspace(0,2*pi,Grid);
[R,TH] = meshgrid(r,th);
Z = 0.1*z(R).*cos(m.*TH);

% Calculate slope (Ggradient components)
[dZr,dZt] = gradient(Z,r,th);
dZt = dZt./(repmat(r(:)',length(th),1));

%% Make plot
% This plots the magnitude of the wave slope, with higher magnitude areas
% appearing darker, and lower magnitude areas appearing lighter. This
% corresponds to experimental images.

% Plot slope magnitude
figure
h1 = surf(R.*cos(TH),R.*sin(TH),Z,abs(sqrt(dZr.^2 + dZt.^2)));
colormap(flipud(gray))
set(h1, 'EdgeColor', 'interp', 'FaceColor', 'interp');
view(2)

% Set axis properties
grid off
set(gca,'visible','off','xtick',[])
set(gca,'YTick',[],'XTick',-1:1:1,'Units','normalized','Position',[0.2 0.1 0.6 0.8],'
    FontSize',9,'FontName','Times')

%% Print
print('waveslopem0n1','-depsc') % Print as an eps file
```

```
76
77 % End timer
78 toc
79
80 % End code
```

Bibliography

[1] J. Kim, "Spray cooling heat transfer: the state of the art," *International Journal of Heat and Fluid Flow*, vol. 28, no. 4, pp. 753–767, 2007.

[2] A. James, B. Vukasinovic, M. Smith, and A. Glezer, "Vibration-induced drop atomization and bursting," *Journal of Fluid Mechanics*, vol. 476, pp. 1–28, 2003.

[3] B. Vukasinovic, M. Smith, and A. Glezer, "Dynamics of a sessile drop in forced vibration," *Journal of Fluid Mechanics*, vol. 587, pp. 395–423, 2007.

[4] C. Tsai, R. Mao, S. Lin, Y. Zhu, and S. Tsai, "Faraday instability-based micro droplet ejection for inhalation drug delivery," *Technology*, vol. 2, no. 01, pp. 75–81, 2014.

[5] P. Chen, Z. Luo, S. Güven, S. Tasoglu, A. Ganesan, A. Weng, and U. Demirci, "Microscale assembly directed by liquid-based template," *Advanced materials*, vol. 26, no. 34, pp. 5936–5941, 2014.

[6] P. Chen, S. Güven, O. Usta, M. Yarmush, and U. Demirci, "Biotunable acoustic node assembly of organoids," *Advanced healthcare materials*, vol. 4, no. 13, pp. 1937–1943, 2015.

[7] S. Guven, P. Chen, F. Inci, S. Tasoglu, B. Erkmen, and U. Demirci, "Multiscale assembly for tissue engineering and regenerative medicine," *Trends in biotechnology*, vol. 33, no. 5, pp. 269–279, 2015.

[8] S. V. Murphy and A. Atala, "3d bioprinting of tissues and organs," *Nature biotechnology*, vol. 32, no. 8, pp. 773–785, 2014.

[9] R. Fan, M. Piou, E. Darling, D. Cormier, J. Sun, and J. Wan, "Bio-printing cell-laden matrigel–agarose constructs," *Journal of Biomaterials Applications*, vol. 31, no. 5, pp. 684–692, 2016.

[10] C. Picard and . Davoust, "Dilational rheology of an air–water interface functionalized by biomolecules: the role of surface diffusion," *Rheologica acta*, vol. 45, no. 4, pp. 497–504, 2006.

[11] C. Picard and L. Davoust, "Resonance frequencies of meniscus waves as a physical mechanism for a dna biosensor," *Langmuir*, vol. 23, no. 3, pp. 1394–1402, 2007.

[12] P. H. Wright and J. R. Saylor, "Patterning of particulate films using faraday waves," *Review of scientific instruments*, vol. 74, no. 9, pp. 4063–4070, 2003.

[13] J. R. Saylor and A. L. Kinard, "Simulation of particle deposition beneath faraday waves in thin liquid films," *Physics of Fluids*, vol. 17, no. 4, p. 047106, 2005.

[14] S. L. Strickland, M. Shearer, and K. E. Daniels, "Spatiotemporal measurement of surfactant distribution on gravity–capillary waves," *Journal of Fluid Mechanics*, vol. 777, pp. 523–543, 2015.

[15] F. Melo, P. Umbanhowar, and H. L. Swinney, "Transition to parametric wave patterns in a vertically oscillated granular layer," *Physical review letters*, vol. 72, no. 1, p. 172, 1994.

[16] A. Briard, L. Gostiaux, and B. Gréa, "The turbulent faraday instability in miscible fluids," *Journal of Fluid Mechanics*, vol. 883, 2020.

[17] A. Shmyrov, A. Mizev, A. Shmyrova, and I. Mizeva, "Capillary wave method: An alternative approach to wave excitation and to wave profile reconstruction," *Physics of Fluids*, vol. 31, no. 1, p. 012101, 2019.

[18] J. R. Saylor, A. J. Szeri, and G. P. Foulks, "Measurement of surfactant properties using a circular capillary wave field," *Experiments in Fluids*, vol. 29, no. 6, pp. 509–518, 2000.

[19] M. Faraday, "Xvii. on a peculiar class of acoustical figures; and on certain forms assumed by groups of particles upon vibrating elastic surfaces," *Philosophical transactions of the Royal Society of London*, vol. 121, pp. 299–340, 1831.

[20] L. Matthiessen, "Akustische versuche, die kleinsten transversalwellen der flüssigkeiten betreffend," *Annalen der Physik*, vol. 210, no. 5, pp. 107–117, 1868.

[21] L. Matthiessen, "Akustische versuche, die kleinsten transversalwellen der flüssigkeiten betreffend," *Annalen der Physik*, vol. 217, no. 11, pp. 375–393, 1870.

[22] L. Rayleigh, "Vii. on the crispations of fluid resting upon a vibrating support," *The London, Edinburgh, and Dublin Philosophical Magazine and Journal of Science*, vol. 16, no. 97, pp. 50–58, 1883.

[23] L. Rayleigh, "Xxxiii. on maintained vibrations," *The London, Edinburgh, and Dublin Philosophical Magazine and Journal of Science*, vol. 15, no. 94, pp. 229–235, 1883.

[24] T. Benjamin and F. Ursell, "The stability of the plane free surface of a liquid in vertical periodic motion," *Proceedings of the Royal Society of London. Series A. Mathematical and Physical Sciences*, vol. 225, no. 1163, pp. 505–115, 1954.

[25] K. Kumar, "Linear theory of faraday instability in viscous liquids," *Proceedings of the Royal Society of London. Series A: Mathematical, Physical and Engineering Sciences*, vol. 452, no. 1948, pp. 1113–1126, 1996.

[26] H. Müller, H. Wittmer, C. Wagnerand, J. Albers, and K. Knorr, "Analytic stability theory for faraday waves and the observation of the harmonic surface response," *Physical review letters*, vol. 78, no. 12, p. 2357, 1997.

[27] W. Edwards and S. Fauve, "Patterns and quasi-patterns in the faraday experiment," *Journal of Fluid Mechanics*, vol. 278, pp. 123–148, 1994.

[28] W. Batson, F. Zoueshtiagh, and R. Narayanan, "Two-frequency excitation of single-mode faraday waves," *Journal of Fluid Mechanics*, vol. 764, pp. 538–571, 2015.

[29] H. Lamb, *Hydrodynamics*. Cambridge University Press, 1932.

[30] B. Christiansen, P. Alstrøm, and M. Levinsen, "Dissipation and ordering in capillary waves at high aspect ratios," *Journal of Fluid Mechanics*, vol. 291, pp. 323–341, 1995.

[31] J. Bechhoefer, V. Ego, S. Manneville, and B. Johnson, "An experimental study of the onset of parametrically pumped surface waves in viscous fluids," *Journal of Fluid Mechanics*, vol. 288, pp. 325–350, 1995.

[32] D. Henderson and J. Miles, "Single-mode faraday waves in small cylinders," *Journal of Fluid Mechanics*, vol. 213, pp. 95–109, 1990.

[33] D. Henderson and J. Miles, "Faraday waves in 2: 1 internal resonance," *Journal of fluid mechanics*, vol. 222, pp. 449–470, 1991.

[34] K. Case and W. Parkinson, "Damping of surface waves in an incompressible liquid," *Journal of Fluid Mechanics*, vol. 2, no. 2, pp. 172–184, 1957.

[35] C. Mei and L. Liu, "The damping of surface gravity waves in a bounded liquid," *Journal of Fluid Mechanics*, vol. 59, no. 2, pp. 239–256, 1973.

[36] S. Douady and S. Fauve, "Pattern selection in faraday instability," *EPL (Europhysics Letters)*, vol. 6, no. 3, p. 221, 1988.

[37] S. Douady, "Experimental study of the faraday instability," *Journal of Fluid Mechanics*, vol. 221, pp. 383–409, 1990.

[38] D. Henderson and J. Miles, "Surface-wave damping in a circular cylinder with a fixed contact line," *Journal of Fluid Mechanics*, vol. 275, pp. 285–299, 1994.

[39] S. Ciliberto and J. Gollub, "Pattern competition leads to chaos," *Physical review letters*, vol. 52, no. 11, p. 922, 1984.

[40] S. Ciliberto and J. Gollub, "Chaotic mode competition in parametrically forced surface waves," *Journal of Fluid Mechanics*, vol. 158, pp. 381–398, 1985.

[41] B. Gluckman, P. Marcq, J. Bridger, and J. Gollub, "Time averaging of chaotic spatiotemporal wave patterns," *Physical review letters*, vol. 71, no. 13, p. 2034, 1993.

[42] C. Martel, J. Nicolas, and J. Vega, "Surface-wave damping in a brimful circular cylinder," *Journal of Fluid Mechanics*, vol. 360, pp. 213–228, 1998.

[43] J. Miles and D. Henderson, "A note on interior vs. boundary-layer damping of surface waves in a circular cylinder," *Journal of Fluid Mechanics*, vol. 364, pp. 319–323, 1998.

[44] S. Davis, "Moving contact lines and rivulet instabilities. part 1. the static rivulet," *Mathematical Proceedings of the Cambridge Philosophical Society*, vol. 98, no. 2, pp. 225–242, 1980.

[45] L. Hocking, "The damping of capillary-gravity waves at a rigid boundary," *Journal of Fluid Mechanics*, vol. 179, pp. 253–266, 1987.

[46] J. Bostwick and P. Steen, "Stability of constrained capillary surfaces," *Annual Review of Fluid Mechanics*, vol. 47, no. 1, pp. 539–568, 2015.

[47] W. Batson, F. Zoueshtiagh, and R. Narayanan, "The faraday threshold in small cylinders and the sidewall non-ideality," *J. Fluid Mech*, vol. 729, no. 496-523, p. 9, 2013.

[48] K. Ward, F. Zoueshtiagh, and R. Narayanan, "Faraday instability in double-interface fluid layers," *Physical Review Fluids*, vol. 4, no. 4, p. 043903, 2019.

[49] R. Kidambi, "Meniscus effects on the frequency and damping of capillarygravity waves in a brimful circular cylinder," *Wave Motion*, vol. 46, no. 2, pp. 144—-154, 2009b.

[50] J. Nicolás, "Effects of static contact angles on inviscid gravity-capillary waves," *Physics of Fluids*, vol. 17, no. 2, p. 022101, 2005.

[51] R. Kidambi, "Capillary damping of inviscid surface waves in a circular cylinder," *Journal of Fluid Mechanics*, vol. 627, pp. 323–340, 2009a.

[52] G. Michel, F. Pétrélis, and S. Fauve, "Acoustic measurement of surface wave damping by a meniscus," *Physical Review Letters*, vol. 116, no. 17, p. 174301, 2016.

[53] J. Miles and D. Henderson, "Parametrically forced surface waves," *Annual Review of Fluid Mechanics*, vol. 22, no. 1, pp. 143–165, 1990.

[54] M. Perlin and W. Schultz, "Capillary effects on surface waves," *Annual review of fluid mechanics*, vol. 32, no. 1, pp. 241–274, 2000.

[55] P. Wilson, X. Shao, J. R. Saylor, and J. B. Bostwick, "Role of edge effects and fluid depth in azimuthal faraday waves," *Phys. Rev. Fluids*, vol. 7, p. 014803, 2022.

[56] X. Shao, P. Wilson, J. Bostwick, and J. Saylor, "Viscoelastic effects in circular edge waves," *Journal of Fluid Mechanics*, vol. 919, p. A18, 2021.

[57] X. Shao, P. Wilson, J. Saylor, and J. Bostwick, "Surface wave pattern formation in a cylindrical container," *Journal of Fluid Mechanics*, vol. 915, p. A19, 2021.

[58] X. Shao, C. Gabbard, J. Bostwick, and J. Saylor, "On the role of meniscus geometry in capillary wave generation," *Experiments in Fluids*, vol. 62, 2021.

[59] X. Shao, G. Bevilacqua, P. Ciarletta, J. Saylor, , and J. Bostwick, "Experimental observation of faraday waves in soft gels," *Physical Review E*, vol. 102, p. 060602(R), 2020.

[60] S. Douady, "Experimental study of the faraday instability," *Journal of Fluid Mechanics*, vol. 221, pp. 383–409, 1990.

[61] K. Kumar and K. M. S. Bajaj, "Competing patterns in the Faraday experiment," *Physical Review E*, vol. 52, no. 5, p. R4606, 1995.

[62] M. Westra, D. J. Binks, and W. Van De Water, "Patterns of Faraday waves," *Journal of Fluid Mechanics*, vol. 496, p. 1, 2003.

[63] T. G. Mezger, *The rheology handbook: for users of rotational and oscillatory rheometers*. Vincentz Network GmbH & Co KG, 2006.

[64] M. Grzelka, J. B. Bostwick, and K. E. Daniels, "Capillary fracture of ultrasoft gels: variability and delayed nucleation," *Soft matter*, vol. 13, no. 16, pp. 2962–2966, 2017.

[65] X. Shao, S. A. Fredericks, J. R. Saylor, and J. B. Bostwick, "Elastocapillary transition in gel drop oscillations," *Physical review letters*, vol. 123, no. 18, p. 188002, 2019.

[66] X. Shao, S. A. Fredericks, J. R. Saylor, and J. B. Bostwick, "A method for determining surface tension, viscosity, and elasticity of gels via ultrasonic levitation of gel drops," *The Journal of the Acoustical Society of America*, vol. 147, no. 4, pp. 2488–2498, 2020.

[67] R. W. Style, A. Jagota, C. Hui, and E. R. Dufresne, "Elastocapillarity: Surface tension and the mechanics of soft solids," *Annual Review of Condensed Matter Physics*, vol. 8, pp. 99–118, 2017.

[68] J. Bico, É. Reyssat, and B. Roman, "Elastocapillarity: When surface tension deforms elastic solids," *Annual Review of Fluid Mechanics*, vol. 50, pp. 629–659, 2018.

[69] X. Shao, J. Saylor, and J. Bostwick, "Extracting the surface tension of soft gels from elastocapillary wave behavior," *Soft Matter*, vol. 14, pp. 7347–7353, 2018.

[70] S. Tamim and J. Bostwick, "The elastic rayleigh drop," *Soft Matter*, vol. 15, p. 9244 – 9252, 2019.

[71] S. Tamim and J. Bostwick, "Oscillations of a soft viscoelastic drop," *npj Microgravity*, vol. 7, p. 42, 2021.

[72] S. Tamim and J. Bostwick, "Plateau-rayleigh instability in a soft viscoelastic material," *Soft Matter*, vol. 17, pp. 4170–4179, 2021.

[73] S. Tamim and J. Bostwick, "A dynamic analysis of the rayleigh-taylor instability in soft solids," *Extreme Mechanics Letters*, vol. 40, p. 100940, 2020.

[74] D. Lyubimov, T. Lyubimova, and S. Shklyaev, "Behavior of a drop on an oscillating solid plate," *Phys. Fluids*, vol. 18, p. 012101, 2006.

[75] J. B. Bostwick and P. H. Steen, "Response of driven sessile drops with contact-line dissipation," *Soft matter*, vol. 12, no. 43, pp. 8919–8926, 2016.

[76] T. Benjamin and J. Scott, "Gravity-capillary waves with edge constraints," *Journal of Fluid Mechanics*, vol. 92, no. 2, pp. 241–267, 1979.

[77] J. Graham-Eagle, "A new method for calculating eigenvalues with applications to gravity-capillary waves with edge constraints," *Mathematical Proceedings of the Cambridge Philosophical Society*, vol. 94, no. 3, pp. 553–564, 1983.

[78] A. Prosperetti, "Linear oscillations of constrained drops, bubbles, and plane liquid surfaces," *Physics of Fluids*, vol. 24, no. 3, p. 032109, 2012.

[79] A. Prosperetti, "Normal-mode analysis for the oscillations of a viscous liquid drop in an immiscible liquid," *Journal de Mecanique*, vol. 19, pp. 149–182, 1980.

[80] J. Bostwick and P. Steen, "Capillary oscillations of a constrained liquid drop," *Physics of Fluids*, vol. 21, p. 032108, 2009.

[81] J. Bostwick and P. Steen, "Coupled oscillations of deformable spherical-cap droplets. part 1. inviscid motions," *Journal of Fluid Mechanics*, vol. 714, pp. 312–335, 2013.

[82] J. Bostwick and P. Steen, "Coupled oscillations of deformable spherical-cap droplets. part 2. viscous motions," *Journal of Fluid Mechanics*, vol. 714, pp. 336–360, 2013.

[83] J. B. Bostwick and P. H. Steen, "Stability of constrained cylindrical interfaces and the torus lift of plateau–rayleigh," *Journal of Fluid Mechanics*, vol. 647, p. 201–219, 2010.

[84] J. B. Bostwick and P. H. Steen, "Liquid bridge shape stability by energy bounding," *IMA Journal of Applied Mathematics*, vol. 80, pp. 1759–1775, 2015.

[85] L. Segel, *Mathematics Applied to Continuum Mechanics*. Dover Publications, 1987.

[86] G. Batchelor, *An Introduction to Fluid Dynamics*. Cambridge University Press, 1967.

[87] S. Chandrasekhar, *Hydrodynamic and Hydromagnetic Stability*. Oxford University Press, 1961.